Mass-Assisted Local Deconfinement in a Confined $\mathbb{Z}_2$ Lattice Gauge Theory

Jean-Yves Desaules,[1,*] Thomas Iadecola,[2,3,†] and Jad C. Halimeh[4,5,6,‡]

[1] *Institute of Science and Technology Austria (ISTA), Am Campus 1, 3400 Klosterneuburg, Austria*
[2] *Department of Physics and Astronomy, Iowa State University, Ames, IA 50011, USA*
[3] *Ames National Laboratory, Ames, IA 50011, USA*
[4] *Department of Physics and Arnold Sommerfeld Center for Theoretical Physics (ASC), Ludwig-Maximilians-Universität München, Theresienstraße 37, D-80333 München, Germany*
[5] *Munich Center for Quantum Science and Technology (MCQST), Schellingstraße 4, D-80799 München, Germany*
[6] *Dahlem Center for Complex Quantum Systems, Freie Universität Berlin, 14195 Berlin, Germany*

(Dated: April 19, 2024)

Confinement is a prominent phenomenon in condensed matter and high-energy physics that has recently become the focus of quantum-simulation experiments of lattice gauge theories (LGTs). As such, a theoretical understanding of the effect of confinement on LGT dynamics is not only of fundamental importance, but can lend itself to upcoming experiments. Here, we show how confinement in a $\mathbb{Z}_2$ LGT can be *locally* avoided by proximity to a resonance between the fermion mass and the electric field strength. Furthermore, we show that this local deconfinement can become global for certain initial conditions, where information transport occurs over the entire chain. In addition, we show how this can lead to strong quantum many-body scarring starting in different initial states. Our findings provide deeper insights into the nature of confinement in $\mathbb{Z}_2$ LGTs and can be tested on current and near-term quantum devices.

Introduction and model.—Lattice gauge theories (LGTs) were originally devised to probe the physics of quark confinement [1], but have since proven to be a useful tool in probing various phenomena in high-energy physics (HEP) [2]. With the advent of quantum simulators of HEP [3–13], it is now possible to directly observe a plethora of HEP features in the laboratory [14–25]. Confinement in LGTs has recently spurred great interest in the quantum-simulation community, with theoretical proposals [26, 27] that have led to direct experimental realization [23].

Another prominent phenomenon seemingly intimately connected to LGTs is quantum many-body scarring (QMBS) [28–35]. Of great interest to studies of ergodicity breaking in interacting models, QMBS relies on the existence of special nonthermal eigenstates equally spaced in energy across the entire spectrum, which is otherwise ergodic [29, 36, 37]. These *scarred* eigenstates have anomalously low bipartite entanglement entropy [36, 38]. Initializing the system in a state having large overlap with these scarred eigenstates leads to long-lived oscillations in the dynamics of local observables, a slow growth in the entanglement entropy, and persistent revivals in the wave function fidelity [28, 33]. QMBS has been the subject of various recent experiments [28, 39–43], and its connection to LGTs has been established in various models [44–57].

$\mathbb{Z}_2$ LGTs have been the subject of substantial interest when it comes to confinement [58–60], including in higher spatial dimensions [61, 62] and at finite temperature [63, 64], and also when it comes to QMBS [45, 51]. Here, we consider the spin-1/2 Hamiltonian

$$\hat{H}=\sum_{j=1}^{L}\left[\frac{J}{2}\left(\hat{X}_j-\hat{Z}_{j-1}\hat{X}_j\hat{Z}_{j+1}\right)+h\hat{Z}_j-\frac{\mu}{2}(-1)^j\hat{Z}_j\hat{Z}_{j+1}\right], \tag{1}$$

with periodic boundary conditions and where $\hat{X}$ and $\hat{Z}$ are Pauli matrices, J is the fermionic hopping strength, μ is the fermionic mass, and h is the electric field strength. This Hamiltonian maps exactly to the $\mathbb{Z}_2$ LGT in a homogeneous gauge sector [58] – see Supplemental Material (SM) [65]. We note that the dynamical term $\hat{X}_j-\hat{Z}_{j-1}\hat{X}_j\hat{Z}_{j+1}$ can be also written as $2\hat{Q}_{j-1}\hat{X}_j\hat{P}_{j+1}+2\hat{P}_{j-1}\hat{X}_j\hat{Q}_{j+1}$ with $\hat{P}_j=(1-\hat{Z}_j)/2=1-\hat{Q}_j$. This means that a spin can be flipped only if its nearest neighbors are in different states. This leads to conservation of the number of Ising domain walls $\hat{N}_{\mathrm{DW}}$, which correspond to fermions in the original LGT. Indeed, while the matter sites have been integrated out, they are still uniquely specified by the configuration of the spins/gauge sites. The fermion density between gauge sites $j, j+1$ is then $\hat{n}_j\equiv(1-\hat{Z}_j\hat{Z}_{j+1})/2$. For clarity, we will use $\downarrow$ and $\uparrow$ to refer to the gauge spins, and $\circ$ (empty) and $\bullet$ (filled) to denote matter. Without loss of generality, we will set $J=1$ and express μ and h in units of J. In the limit of $h\gg\mu,J$, the model experiences strong confinement and the only allowed motion is the hopping of mesons (particle-antiparticle pairs) [58, 66]. However, that process only happens at second order and so is suppressed by a factor of J^2/h. As such, in the limit of $h\to\infty$, the system is completely frozen.

In this Letter, we show that adding a very large mass $\mu\approx h$ counterintuitively leads to deconfinement. While

* jean-yves.desaules@ist.ac.at
† iadecola@iastate.edu
‡ jad.halimeh@physik.lmu.de

this deconfinement is generally only local, from certain initial states information can propagate throughout the chain, exhibiting *global* deconfinement. We also show that the effective dynamics at $\mu = h$ leads to perfect revivals from several states. Importantly, due to the special interplay of higher-order perturbative corrections, this leads to QMBS in the full model already for $\mu = h \approx J$.

Mass Resonance and deconfinement.—To understand the effective dynamics when $\mu = h$, we set $h = \mu$ in Eq. (1) and rewrite it as $\hat{H} = \mu(\hat{H}_0 + \lambda\hat{V})$, where $\hat{H}_0 = \sum_j [\hat{Z}_j - (-1)^j \hat{Z}_j\hat{Z}_{j+1}/2]$, $\hat{V} = \frac{1}{2}\sum_j (\hat{X}_j - \hat{Z}_{j-1}\hat{X}_j\hat{Z}_{j+1})$, and $\lambda = J/\mu$. Taking the limit $\mu \to \infty$, we perform a Schrieffer-Wolff (SW) [67] transformation to obtain an effective Hamiltonian with an emergent conservation law for $\hat{H}_0$. The leading-order contribution is $\mathcal{O}(\lambda)$ and obtained by projecting $\hat{V}$ into a degenerate eigenspace of $\hat{H}_0$:

$$\hat{H}_{\text{eff}} = J \sum_{j \text{ odd}} \hat{Q}_{j-1}\hat{X}_j\hat{P}_{j+1} + J \sum_{j \text{ even}} \hat{P}_{j-1}\hat{X}_j\hat{Q}_{j+1}. \quad (2)$$

This Hamiltonian can be understood as only keeping processes where the change of energy due to h is exactly compensated by that due to the mass term μ. It is worth noting that $\hat{H}_{\text{eff}}$ can be turned into a translation-invariant Hamiltonian using the unitary transformation $\prod_{j \text{ even}} \hat{X}_j$. We then have simply $\hat{H}_{\text{eff}} = \sum_j \hat{P}_{j-1}\hat{X}_j\hat{Q}_{j+1}$. This model is reminiscent of the classical cellular automaton with rule 156 [68]. This kinetically constrained model was recently also considered in Ref. [69], where a few of its properties were discussed. We will discuss these in the language of our spin model and in the context of LGTs, as well a show a few additional ones.

$\hat{H}_{\text{eff}}$ conserves the number of domain walls and $\hat{H}_0$ by construction, but furthermore exhibits Hilbert space fragmentation [70, 71] within each of these symmetry sectors. This can be understood due to the emergence of an extensive number of local conserved quantities $\hat{O}_j$ defined as (see SM [65] for more details)

$$\hat{O}_j = \begin{cases} \hat{Q}_j\hat{Q}_{j+1}, & \text{for } j \text{ odd} \\ \hat{P}_j\hat{P}_{j+1}, & \text{for } j \text{ even.} \end{cases} \quad (3)$$

Each $O_j = \langle\hat{O}_j\rangle$ can be either 0 or 1, but it is simple to see that if O_j is 1 then sites j and $j+1$ must be up and so both O_{j-1} and O_{j+1} must be 0. This allows to compute the number of possible configurations of the O_j as $\mathcal{F}_{L-1} + \mathcal{F}_{L+1} + 1$, where $\mathcal{F}_n$ is the n^{th} Fibonacci number [65]. Almost all disconnected sectors can uniquely be identified from values of the O_j. The only exception are the two Néel states $|\cdots\uparrow\downarrow\uparrow\downarrow\cdots\rangle$, which are both frozen despite having $O_j = 0$ for all j.

Beyond this fragmentation, $\hat{H}_{\text{eff}}$ is in fact integrable. Dynamics only arise when a few consecutive $O_j = 0$. This is because $O_j = 1$ (for j odd) implies $\uparrow\uparrow$ while $O_j = 0$ allows for some freedom as it is satisfied by $\uparrow\downarrow$, $\downarrow\uparrow$, or $\downarrow\downarrow$ (and similarly for j even). If we consider $O_k = O_{k+r} = 1$ but $O_j = 0$ for $k < j < k + r$, then we have $r - 2$ sites that can change. These states are not free, as they must respect $O_j = 0$. So between the two frozen blocks, the state must locally resemble a Néel state with no $\uparrow\uparrow$ or $\downarrow\downarrow$. However, as we can still have $\downarrow\downarrow$ on odd-even sites and $\uparrow\uparrow$ on even-odd sites, we can actually have two different Néel domains and move the boundary between them [65]. As such, we have an effective tight-binding chain with hopping rate J and with $r - 1$ sites, which is integrable. As the full dynamics is just composed of all disconnected parts evolving on their own, this means that $\hat{H}_{\text{eff}}$ is integrable. This picture also allows us to compute the number of states in each O_j sector by simply multiplying the number of states in each tight-binding chain.

We now look at this tight-binding chain from the vantage point of the LGT. Between any two frozen blocks, there is a single mobile quasiparticle corresponding to the absence of a domain wall. In LGT language, this quasiparticle is simply a hole in a fully packed matter background. If we focus on the sector with only $O_1 = 1$, this hole can travel freely along the *entirety* of the chain, even for $h = \mu \to \infty$. This is surprising, as in the limit $h \to \infty$ the system is completely frozen due to confinement [58]. Thus, adding a very large mass actually favors the mobility of holes, despite intuition suggesting the opposite. We emphasize that this is not a generic feature. For example, in the spin-1/2 U(1) quantum link model [72, 73], a similar resonance between mass and confining potential arises. While it also locally unfreezes the system, the resulting dynamics is strictly local and information cannot propagate along the chain [74].

QMBS away from integrability.—Due to the solvability of the model, it is straightforward to engineer states that exhibit periodic dynamics in the limit of $h{=}\mu{\to}\infty$. For that, we need to restrict to sectors where all eigenvalues are equally spaced. This in turn implies that they need to be equally spaced in each disconnected part of the chain. However, for a tight-binding chain with equal coupling the eigenvalues are only equidistant for 1, 2, or 3 sites [75]. For a chain with 1 site, everything is trivial as there is no dynamics and we avoid such cases. As the hopping strength is J, in the two-site case the eigenvalues are $\pm J$ while in the three-site case they are $\pm\sqrt{2}J$ and 0. As the energy spacings are not commensurate, we expect periodic dynamics in the full system only if we have a single type of chains. In that case, we can map every frozen domain with two or three states to a spin-1/2 and a spin-1, respectively. We can then identify three simple initial states that correspond to charge density waves (CDWs) for the matter sites. These states are $|\Psi_2\rangle = |\downarrow\uparrow\uparrow\downarrow\downarrow\uparrow\uparrow\downarrow\cdots\rangle = |\bullet\circ\bullet\circ\cdots\rangle$, $|\Psi_3\rangle = |\downarrow\downarrow\uparrow\uparrow\uparrow\downarrow\downarrow\downarrow\uparrow\uparrow\uparrow\downarrow\cdots\rangle = |\circ\bullet\circ\circ\bullet\circ\cdots\rangle$, and $|\Psi_4\rangle = |\downarrow\downarrow\uparrow\downarrow\downarrow\downarrow\uparrow\downarrow\cdots\rangle = |\circ\bullet\bullet\circ\circ\bullet\bullet\circ\cdots\rangle$, where red denotes that a site is frozen. The state $|\Psi_3\rangle$ lives in a sector with $N/3$ effective spins-1/2, as each unfrozen site can freely flip between 0 and 1. Meanwhile, both $|\Psi_2\rangle$

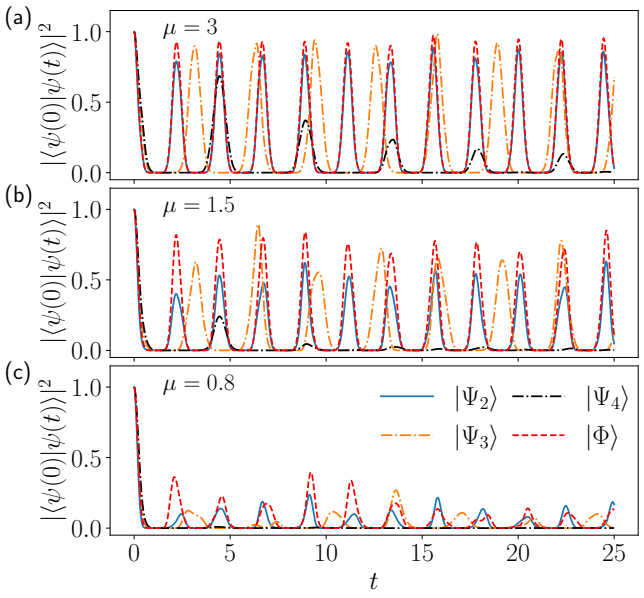

FIG. 1. Quenches from different initial states for (a) $\mu = h = 3J$, (b) $\mu = h = 1.5J$ and (c) $\mu = h = 3J$. The system size used is $L = 20$ for all states except for $|\Psi_3\rangle$ where we use $L = 18$ instead. While all states show good revivals for large values of $\mu/J = h/J$, this is no longer true when all parameters are comparable.

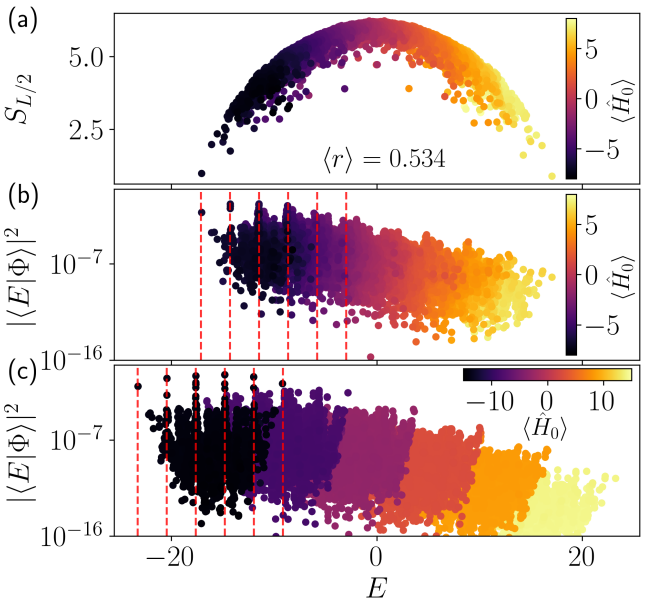

FIG. 2. Eigenstate properties for $L = 20$ and 10 domain-walls, with (a)-(b) $\mu = h = 0.8J$ and (c) $\mu = h = 1.5J$. In all panels, the color indicates the expectation value of $\hat{H}_0$. (a) Entanglement entropy of eigenstates in the sector symmetric under translation by two sites and spatial inversion. The profile and mean energy-level spacing [76, 77] are fairly typical of chaotic systems. (b)-(c) Overlap between the $|\Phi\rangle$ state and the eigenstates for two different values of $\mu = h$. In both panels, the red dashed lines are spaced by $\sqrt{8}J$ as expected from the spin-1 picture.

and $|\Psi_4\rangle$ live in the same sector with $N/4$ effective spins-1. In each unfrozen part of the chain, only the three states $|\uparrow\downarrow\rangle \equiv |-1\rangle$, $|\uparrow\uparrow\rangle \equiv |0\rangle$ and $|\downarrow\uparrow\rangle \equiv |+1\rangle$ are allowed. Thus $|\Psi_2\rangle$ is akin to $|0, 0, 0, \ldots\rangle$ in the spin-1 language while $|\Psi_4\rangle$ is akin to $|+1, +1, +1, \ldots\rangle$. This means that $|\Psi_2\rangle$ will lead to state transfer to the entangled state where each spin-1 is in a superposition of $|+1\rangle$ and $|-1\rangle$, meaning that each cell is $(|\downarrow\uparrow\downarrow\downarrow\rangle + |\downarrow\downarrow\uparrow\downarrow\rangle)/\sqrt{2}$. This state will also be important in the dynamics and we denote it by $|\Phi\rangle$.

Fig. 1 shows the fidelity $|\langle\psi(0)|\psi(t)\rangle|^2$ after a quench from these four states. While they all revive well for large values of $\mu = h$, their behavior differs greatly when μ and h are of the order of J. In particular, $|\Psi_4\rangle$ revivals disappear quickly while $|\Phi\rangle$ shows clean oscillations even at $\mu = h = 0.8J$. This is surprising, as for these values of the parameters the system is not separated into sectors of $\hat{H}_0$ and is chaotic, as demonstrated by the entanglement entropy of the eigenstates and mean energy spacing in Fig. 2(a). Nonetheless, Fig. 2(b) demonstrates that the overlap of these eigenstates with $|\Phi\rangle$ still shows some regular structure consistent with the spin-1 approach. This becomes clearer as $\mu = h$ is increased to $1.5J$, along with the different sectors separating.

The faster decay of revivals of $|\Psi_3\rangle$ compared to $|\Phi\rangle$ can be understood from the influence of the other sectors of $\hat{H}_0$ [65]. However, we will show that this is not the case when comparing $|\Phi\rangle$ and $|\Psi_4\rangle$. To this end, we define the projector $\hat{\mathcal{P}}_1$ onto the spin-1 sector and the projector $\hat{\mathcal{P}}_{H_0}$ onto all states with the same expectation value of $\hat{H}_0$ as $|\Phi\rangle$ (or, correspondingly, as $|\Psi_2\rangle$ or $|\Psi_4\rangle$). Fig. 3(a) clearly shows that $\hat{\mathcal{P}}_{H_0}$ is very similar for both $|\Phi\rangle$ and $|\Psi_4\rangle$, but that $\hat{\mathcal{P}}_1$ is not. Thus, the difference between these states results from the intra-sector dynamics generated by higher-order SW terms.

Beyond first order.— While $\hat{H}_{\text{eff}}$ provides an exact description of the dynamics for infinite $\mu = h$, higher-order terms in the SW transformation are needed for finite values of these two parameters. The term at second order reads

$$\begin{aligned} H^{(2)}_{\text{eff}} = \frac{J^2}{4\mu}\Big[&\sum_{j \text{ even}} \hat{Q}_{j-1}(\hat{\sigma}^+_j\hat{\sigma}^-_{j+1} + \hat{\sigma}^-_j\hat{\sigma}^+_{j+1})\hat{Q}_{j+2} \\ &- \sum_{j \text{ odd}} \hat{P}_{j-1}(\hat{\sigma}^+_j\hat{\sigma}^-_{j+1} + \hat{\sigma}^-_j\hat{\sigma}^+_{j+1})\hat{P}_{j+2} \\ &+ \sum_{j \text{ even}} \hat{Q}_{j-1}\hat{Z}_j\hat{P}_{j+1} + \sum_{j \text{ odd}} \hat{P}_{j-1}\hat{Z}_j\hat{Q}_{j+1}\Big]. \end{aligned} \tag{4}$$

While the third-order term is nonzero [65], its prefactor is $J^3/(32\mu^2)$; thus, even if $J/\mu \approx 1$, it is already highly suppressed. As such, our analysis will concentrate on the second-order term.

$\hat{H}^{(2)}_{\text{eff}}$ does not commute with the $\hat{O}_j$ operators. It can for example take the state $|\downarrow\downarrow\uparrow\downarrow\downarrow\downarrow\rangle$ to $|\downarrow\downarrow\downarrow\uparrow\downarrow\downarrow\rangle$, thus changing the value of $\hat{O}_2 = \hat{P}_2\hat{P}_3$ an $\hat{O}_4 = \hat{P}_4\hat{P}_5$. So

we expect the resulting model to be fully ergodic, but this depends on the filling factor. For example, in the $(\hat{H}_0, \hat{N}_{\rm DW})$ sector of $|\Psi_3\rangle$, the three effective spin-1/2 sectors are annihilated by $\hat{H}^{(2)}_{\rm eff}$ and remain disconnected from the rest of the chain. Nonetheless, in the sector containing $|\Psi_2\rangle$, $|\Psi_4\rangle$, and $|\Phi\rangle$, the picture is different. For L divisible by 4 with $L/2$ domain walls, we find that the Hamiltonian is fully connected in the computational basis. The level statistics are also Wigner-Dyson for $\mu{>}0.5J$ [65], demonstrating that $\hat{H}^{(2)}_{\rm eff}$ completely destroys the integrability of $\hat{H}_{\rm eff}$.

In the spin-1 sector, the diagonal part of $\hat{H}^{(2)}_{\rm eff}$ can lead to decay of revivals from $|\Psi_4\rangle$, but this can be compensated by the detuning between h and μ [65]. In any case, this effect is small when compared to the action of the off-diagonal terms of $\hat{H}^{(2)}_{\rm eff}$. While they do not connect any pair of states within the spin-1 sector, they lead to leakage out of it. This is reminiscent of QMBS observed in Refs. [42, 78]. In these works, there is also an effective spin-1 or spin-1/2 sector with additional terms creating leakage. In both cases, there are only revivals from the states that do not directly leak out of the regular sector. The dynamics is then simply state transfer between these two special states. In our model, there is only a single state with no leakage caused by $\hat{H}^{(2)}_{\rm eff}$, which is $|\Psi_2\rangle$. However, it leads to state transfer to the state $|\Phi\rangle$, which has *maximum* leakage in the spin-1 sector. The fact that this does not prevent $|\Psi_2\rangle$ from reviving and that $|\Phi\rangle$ has even better revivals means that this simple picture of leakage is not enough to understand the dynamics.

We cannot simply consider the rest of the Hilbert space as a kind of "reservoir" from which no information comes back. Instead, we have to look at where $\hat{H}^{(2)}_{\rm eff}$ takes it. Importantly, for $\mu{\geq}0.5J$, we find that instead of spreading into the full Hilbert space, the wave function remains close to the spin-1 subsector. Let us denote by "neighbor states" all computational basis states in the Krylov subspaces of $\hat{H}_{\rm eff}$ that can be reached from the spin-1 subsector with a *single* application of $\hat{H}^{(2)}_{\rm eff}$. We find that when evolving $|\Phi\rangle$ with $\hat{H}_{\rm eff} + \hat{H}^{(2)}_{\rm eff}$, even if the wave function leaves the spin-1 subsector, it essentially entirely remains within the "neighbor states". To show this, we can define the projector $\hat{\mathcal{P}}_2$ onto "neighbor states" and states in the spin-1 subsector. Fig. 3(b) shows that the expectation value of this projector essentially remains at 1, even as $\hat{\mathcal{P}}_1$ itself oscillates. In fact, we find that within the "neighbor states" the wave function concentrates into a small subset of states. These take the form of $|{\downarrow}{\uparrow\uparrow}{\downarrow}\cdots{\downarrow}{\uparrow\uparrow}{\downarrow\downarrow\downarrow\downarrow}{\uparrow\downarrow}{\uparrow\uparrow}{\downarrow}\rangle$ and its equivalents under all possible translations (by an even number of sites) and under spatial inversion. We will denote by $|\beta\rangle$ the symmetric superposition of these $L/2$ states. An important property of these states is that applying $\hat{H}^{(2)}_{\rm eff}$ to them only leads to the spin-1 subsector and does not lead to leakage further away from it. This explains why the wave function does not spread into the full Hilbert space. Meanwhile, after a quench from $|\Psi_4\rangle$, the wave function spreads into more "neighbor states" and leaks further into the rest of the Hilbert space. This is caused by the lack of destructive interference due to the absence of the partner state with $|{\downarrow}\uparrow{\downarrow}\uparrow{\downarrow}\rangle$ in each cell [65].

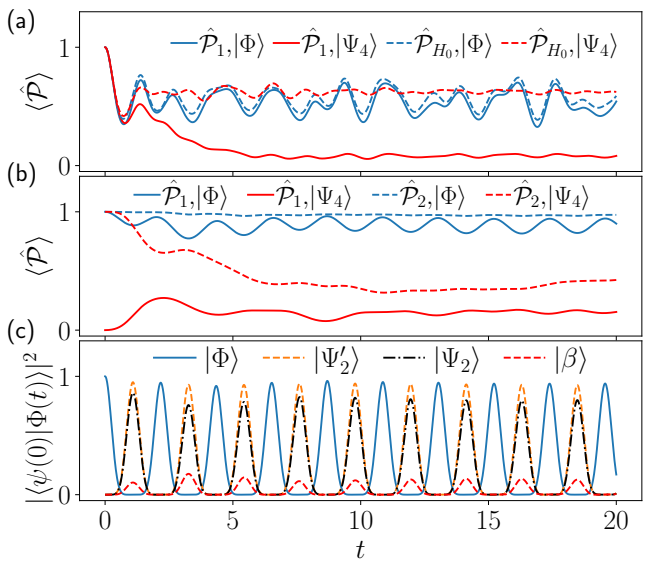

FIG. 3. Expectation value of projectors and overlap after quenches for $L = 16$ and $\mu = h = J$. (a) When the system is evolved with the full Hamiltonian, for both initial states the amount of the wave function remaining in the "correct" sector of $\hat{H}_0$ is similar, but this is not at all true for the spin-1 sector. This means that the main difference is to be found in the effective dynamics in the sector. So in panel (b), the states are evolved with $\hat{H}_{\rm eff} + \hat{H}^{(2)}_{\rm eff}$. For $|\Phi\rangle$ the wave function escaping the spin-1 sector is almost entirely going to the "neighbor states". (c) More precisely, all the wave function outside of the spin-1 sector concentrates on $|\beta\rangle$. At half the period, the quantum state is $|\Psi_2'\rangle$ with more than 95% fidelity.

As for the dynamics of $|\Phi\rangle$ under $\hat{H}_{\rm eff}{+}\hat{H}^{(2)}_{\rm eff}$, Fig. 3(c) shows that the wave function has nonnegligible overlap with $|\beta\rangle$ after a half-period. This means that for $\mu{\geq}0.5J$, $\hat{H}^{(2)}_{\rm eff}$ does not destroy the periodic revivals of $|\Phi\rangle$, but rather deforms its trajectory. The state at half the period then goes from $|\Psi_2\rangle$ (at $\mu{=}h{=}\infty$) to $|\Psi_2'\rangle = (|\Psi_2\rangle - \alpha\,|\beta\rangle)/\sqrt{1{+}\alpha^2}$, with α a smooth function o μ. This is shown clearly in Fig. 3(c). Using the full Hamiltonian in Eq. 1 at finite μ, we also find an increased revival fidelity when quenching from $|\Psi_2'\rangle$ instead of $|\Psi_2\rangle$, with an optimal α of $\alpha^\star(\mu){\approx}1/(0.46{+}2.58\mu/J)$ [65].

Summary and outlook.— In this Letter, we have explored adding a resonant mass term to a strongly confined $\mathbb{Z}_2$ LGT. The mass term has the counterintuitive effect of inducing *local* deconfinement such that a single hole within a fully packed matter background becomes mobile. In the extreme limit where only a single hole is present, information can propagate across the system; otherwise, the holes remain spatially confined to local regions of varying sizes, each of which constitutes an in-

dependent tight-binding chain. For certain CDW matter configurations where these tight-binding chains have commensurate spectra, this structure gives rise to periodic fidelity revivals. These features are sharp in the limit $\mu{=}h{=}\infty$, where the model becomes integrable. Remarkably, when integrability breaking perturbative corrections are included that weaken many of these effects, a particular period-2 CDW state continues to exhibit robust fidelity revivals even for modest $\mu{\sim}h{\sim}J$. We trace these revivals back to destructive interference along the Hilbert space trajectory of the initial state, made possible by the intricate interplay between the first and second terms of the effective Hamiltonian. This leads to the periodic trajectory of the integrable limit being smoothly deformed instead of breaking down as $\mu/J = h/J$ is decreased. This is unlike previous examples of QMBS surviving from an integrable regime, where the regular dynamics relied simply on the trajectory being mostly annihilated by higher-order corrections. This provides a new mechanism for QMBS in the $\mathbb{Z}_2$ LGT, and in models with an integrable limit in general.

Signatures of these QMBS, including oscillations of the matter imbalance [65], are readily observable in present-day quantum simulators. The model (1), including the mass term, can be realized as a limit of the mixed-field Ising model [51, 79], making trapped-ion and Rydberg-atom platforms particularly well suited. Furthermore, it is interesting to ask whether the local deconfinement mechanism explored in this paper is generic to $\mathbb{Z}_2$ LGTs in higher dimensions, or whether it arises for other gauge groups. Indeed, the absence of this mechanism in the U(1) quantum link model [74] begs the question of what are the necessary and sufficient conditions for this behavior to occur. Understanding this will shed light on the nature of confinement and on mechanisms to avoid it.

Acknowledgments.— The authors are grateful to Fiona Burnell, Gaurav Gyawali, Zlatko Papić, Elliot Rosenberg, Pedram Roushan, and Michael Schecter for insightful discussions. J.-Y.D. acknowledges funding from the European Union's Horizon 2020 research and innovation programme under the Marie Skłodowska-Curie Grant Agreement No. 101034413. T.I. acknowledges support from the National Science Foundation under Grant No. DMR-2143635. J.C.H. acknowledges support from the Emmy Noether Programme of the German Research Foundation (DFG) under grant no. HA 8206/1-1.

[1] Kenneth G. Wilson, "Confinement of quarks," Phys. Rev. D **10**, 2445–2459 (1974).
[2] H.J. Rothe, *Lattice Gauge Theories: An Introduction*, EBSCO ebook academic collection (World Scientific, 2005).
[3] M. Dalmonte and S. Montangero, "Lattice gauge theory simulations in the quantum information era," Contemporary Physics **57**, 388–412 (2016).
[4] Mari Carmen Bañuls, Rainer Blatt, Jacopo Catani, Alessio Celi, Juan Ignacio Cirac, Marcello Dalmonte, Leonardo Fallani, Karl Jansen, Maciej Lewenstein, Simone Montangero, Christine A. Muschik, Benni Reznik, Enrique Rico, Luca Tagliacozzo, Karel Van Acoleyen, Frank Verstraete, Uwe-Jens Wiese, Matthew Wingate, Jakub Zakrzewski, and Peter Zoller, "Simulating lattice gauge theories within quantum technologies," The European Physical Journal D **74**, 165 (2020).
[5] Erez Zohar, J Ignacio Cirac, and Benni Reznik, "Quantum simulations of lattice gauge theories using ultracold atoms in optical lattices," Reports on Progress in Physics **79**, 014401 (2015).
[6] Yuri Alexeev, Dave Bacon, Kenneth R. Brown, Robert Calderbank, Lincoln D. Carr, Frederic T. Chong, Brian DeMarco, Dirk Englund, Edward Farhi, Bill Fefferman, Alexey V. Gorshkov, Andrew Houck, Jungsang Kim, Shelby Kimmel, Michael Lange, Seth Lloyd, Mikhail D. Lukin, Dmitri Maslov, Peter Maunz, Christopher Monroe, John Preskill, Martin Roetteler, Martin J. Savage, and Jeff Thompson, "Quantum computer systems for scientific discovery," PRX Quantum **2**, 017001 (2021).
[7] Monika Aidelsburger, Luca Barbiero, Alejandro Bermudez, Titas Chanda, Alexandre Dauphin, Daniel González-Cuadra, Przemysław R. Grzybowski, Simon Hands, Fred Jendrzejewski, Johannes Jünemann, Gediminas Juzeliūnas, Valentin Kasper, Angelo Piga, Shi-Ju Ran, Matteo Rizzi, Germán Sierra, Luca Tagliacozzo, Emanuele Tirrito, Torsten V. Zache, Jakub Zakrzewski, Erez Zohar, and Maciej Lewenstein, "Cold atoms meet lattice gauge theory," Philosophical Transactions of the Royal Society A: Mathematical, Physical and Engineering Sciences **380**, 20210064 (2022).
[8] Erez Zohar, "Quantum simulation of lattice gauge theories in more than one space dimension: requirements, challenges and methods," Philosophical Transactions of the Royal Society A: Mathematical, Physical and Engineering Sciences **380**, 20210069 (2022).
[9] Natalie Klco, Alessandro Roggero, and Martin J Savage, "Standard model physics and the digital quantum revolution: thoughts about the interface," Reports on Progress in Physics **85**, 064301 (2022).
[10] Christian W. Bauer, Zohreh Davoudi, A. Baha Balantekin, Tanmoy Bhattacharya, Marcela Carena, Wibe A. de Jong, Patrick Draper, Aida El-Khadra, Nate Gemelke, Masanori Hanada, Dmitri Kharzeev, Henry Lamm, Ying-Ying Li, Junyu Liu, Mikhail Lukin, Yannick Meurice, Christopher Monroe, Benjamin Nachman, Guido Pagano, John Preskill, Enrico Rinaldi, Alessandro Roggero, David I. Santiago, Martin J. Savage, Irfan Siddiqi, George Siopsis, David Van Zanten, Nathan Wiebe, Yukari Yamauchi, Kübra Yeter-Aydeniz, and Silvia Zorzetti, "Quantum simulation for high-energy physics," PRX Quantum **4**, 027001 (2023).
[11] Alberto Di Meglio, Karl Jansen, Ivano Tavernelli, Constantia Alexandrou, Srinivasan Arunachalam, Christian W. Bauer, Kerstin Borras, Stefano Carrazza, Arianna Crippa, Vincent Croft, Roland de Putter, Andrea Delgado, Vedran Dunjko, Daniel J. Egger, Elias Fernandez-Combarro, Elina Fuchs, Lena Funcke, Daniel

Gonzalez-Cuadra, Michele Grossi, Jad C. Halimeh, Zoe Holmes, Stefan Kuhn, Denis Lacroix, Randy Lewis, Donatella Lucchesi, Miriam Lucio Martinez, Federico Meloni, Antonio Mezzacapo, Simone Montangero, Lento Nagano, Voica Radescu, Enrique Rico Ortega, Alessandro Roggero, Julian Schuhmacher, Joao Seixas, Pietro Silvi, Panagiotis Spentzouris, Francesco Tacchino, Kristan Temme, Koji Terashi, Jordi Tura, Cenk Tuysuz, Sofia Vallecorsa, Uwe-Jens Wiese, Shinjae Yoo, and Jinglei Zhang, "Quantum computing for high-energy physics: State of the art and challenges. summary of the QC4HEP working group," arXiv eprints (2023), arXiv:2307.03236 [quant-ph].

[12] Jad C. Halimeh, Monika Aidelsburger, Fabian Grusdt, Philipp Hauke, and Bing Yang, "Cold-atom quantum simulators of gauge theories," arXiv eprints (2023), arXiv:2310.12201 [cond-mat.quant-gas].

[13] Yanting Cheng and Hui Zhai, "Emergent gauge theory in Rydberg atom arrays," arXiv eprints (2024), arXiv:2401.07708 [cond-mat.quant-gas].

[14] Esteban A. Martinez, Christine A. Muschik, Philipp Schindler, Daniel Nigg, Alexander Erhard, Markus Heyl, Philipp Hauke, Marcello Dalmonte, Thomas Monz, Peter Zoller, and Rainer Blatt, "Real-time dynamics of lattice gauge theories with a few-qubit quantum computer," Nature **534**, 516–519 (2016).

[15] N. Klco, E. F. Dumitrescu, A. J. McCaskey, T. D. Morris, R. C. Pooser, M. Sanz, E. Solano, P. Lougovski, and M. J. Savage, "Quantum-classical computation of Schwinger model dynamics using quantum computers," Phys. Rev. A **98**, 032331 (2018).

[16] Frederik Görg, Kilian Sandholzer, Joaquín Minguzzi, Rémi Desbuquois, Michael Messer, and Tilman Esslinger, "Realization of density-dependent Peierls phases to engineer quantized gauge fields coupled to ultracold matter," Nature Physics **15**, 1161–1167 (2019).

[17] Christian Schweizer, Fabian Grusdt, Moritz Berngruber, Luca Barbiero, Eugene Demler, Nathan Goldman, Immanuel Bloch, and Monika Aidelsburger, "Floquet approach to $\mathbb{Z}2$ lattice gauge theories with ultracold atoms in optical lattices," Nature Physics **15**, 1168–1173 (2019).

[18] Alexander Mil, Torsten V. Zache, Apoorva Hegde, Andy Xia, Rohit P. Bhatt, Markus K. Oberthaler, Philipp Hauke, Jürgen Berges, and Fred Jendrzejewski, "A scalable realization of local U(1) gauge invariance in cold atomic mixtures," Science **367**, 1128–1130 (2020).

[19] Bing Yang, Hui Sun, Robert Ott, Han-Yi Wang, Torsten V. Zache, Jad C. Halimeh, Zhen-Sheng Yuan, Philipp Hauke, and Jian-Wei Pan, "Observation of gauge invariance in a 71-site Bose–Hubbard quantum simulator," Nature **587**, 392–396 (2020).

[20] Zhan Wang, Zi-Yong Ge, Zhongcheng Xiang, Xiaohui Song, Rui-Zhen Huang, Pengtao Song, Xue-Yi Guo, Luhong Su, Kai Xu, Dongning Zheng, and Heng Fan, "Observation of emergent $\mathbb{Z}_2$ gauge invariance in a superconducting circuit," Phys. Rev. Research **4**, L022060 (2022).

[21] Zhao-Yu Zhou, Guo-Xian Su, Jad C. Halimeh, Robert Ott, Hui Sun, Philipp Hauke, Bing Yang, Zhen-Sheng Yuan, Jürgen Berges, and Jian-Wei Pan, "Thermalization dynamics of a gauge theory on a quantum simulator," Science **377**, 311–314 (2022).

[22] Julius Mildenberger, Wojciech Mruczkiewicz, Jad C. Halimeh, Zhang Jiang, and Philipp Hauke, "Probing confinement in a $\mathbb{Z}_2$ lattice gauge theory on a quantum computer," arXiv eprints (2022), arXiv:2203.08905 [quant-ph].

[23] Wei-Yong Zhang, Ying Liu, Yanting Cheng, Ming-Gen He, Han-Yi Wang, Tian-Yi Wang, Zi-Hang Zhu, Guo-Xian Su, Zhao-Yu Zhou, Yong-Guang Zheng, Hui Sun, Bing Yang, Philipp Hauke, Wei Zheng, Jad C. Halimeh, Zhen-Sheng Yuan, and Jian-Wei Pan, "Observation of microscopic confinement dynamics by a tunable topological θ-angle," arXiv eprints (2023), arXiv:2306.11794 [cond-mat.quant-gas].

[24] Roland C. Farrell, Marc Illa, Anthony N. Ciavarella, and Martin J. Savage, "Scalable circuits for preparing ground states on digital quantum computers: The Schwinger model vacuum on 100 qubits," arXiv eprints (2023), arXiv:2308.04481 [quant-ph].

[25] Takis Angelides, Pranay Naredi, Arianna Crippa, Karl Jansen, Stefan Kühn, Ivano Tavernelli, and Derek S. Wang, "First-order phase transition of the Schwinger model with a quantum computer," arXiv eprints (2023), arXiv:2312.12831 [hep-lat].

[26] Jad C. Halimeh, Ian P. McCulloch, Bing Yang, and Philipp Hauke, "Tuning the topological θ-angle in cold-atom quantum simulators of gauge theories," PRX Quantum **3**, 040316 (2022).

[27] Yanting Cheng, Shang Liu, Wei Zheng, Pengfei Zhang, and Hui Zhai, "Tunable confinement-deconfinement transition in an ultracold-atom quantum simulator," PRX Quantum **3**, 040317 (2022).

[28] Hannes Bernien, Sylvain Schwartz, Alexander Keesling, Harry Levine, Ahmed Omran, Hannes Pichler, Soonwon Choi, Alexander S. Zibrov, Manuel Endres, Markus Greiner, Vladan Vuletić, and Mikhail D. Lukin, "Probing many-body dynamics on a 51-atom quantum simulator," Nature **551**, 579–584 (2017).

[29] C. J. Turner, A. A. Michailidis, D. A. Abanin, M. Serbyn, and Z. Papić, "Weak ergodicity breaking from quantum many-body scars," Nature Physics **14**, 745–749 (2018).

[30] Sanjay Moudgalya, Stephan Rachel, B. Andrei Bernevig, and Nicolas Regnault, "Exact excited states of nonintegrable models," Phys. Rev. B **98**, 235155 (2018).

[31] Hongzheng Zhao, Joseph Vovrosh, Florian Mintert, and Johannes Knolle, "Quantum many-body scars in optical lattices," Phys. Rev. Lett. **124**, 160604 (2020).

[32] Paul Niklas Jepsen, Yoo Kyung 'Eunice' Lee, Hanzhen Lin, Ivana Dimitrova, Yair Margalit, Wen Wei Ho, and Wolfgang Ketterle, "Long-lived phantom helix states in Heisenberg quantum magnets," Nature Physics **18**, 899–904 (2022).

[33] Maksym Serbyn, Dmitry A. Abanin, and Zlatko Papić, "Quantum many-body scars and weak breaking of ergodicity," Nature Physics **17**, 675–685 (2021).

[34] Sanjay Moudgalya, B Andrei Bernevig, and Nicolas Regnault, "Quantum many-body scars and Hilbert space fragmentation: a review of exact results," Reports on Progress in Physics **85**, 086501 (2022).

[35] Anushya Chandran, Thomas Iadecola, Vedika Khemani, and Roderich Moessner, "Quantum many-body scars: A quasiparticle perspective," Annual Review of Condensed Matter Physics **14**, 443–469 (2023).

[36] Sanjay Moudgalya, Nicolas Regnault, and B. Andrei Bernevig, "Entanglement of exact excited states of Affleck-Kennedy-Lieb-Tasaki models: Exact results, many-body scars, and violation of the strong eigenstate

thermalization hypothesis," Phys. Rev. B **98**, 235156 (2018).
[37] Michael Schecter and Thomas Iadecola, "Weak ergodicity breaking and quantum many-body scars in spin-1 XY magnets," Phys. Rev. Lett. **123**, 147201 (2019).
[38] Cheng-Ju Lin and Olexei I. Motrunich, "Exact quantum many-body scar states in the Rydberg-blockaded atom chain," Phys. Rev. Lett. **122**, 173401 (2019).
[39] D. Bluvstein, A. Omran, H. Levine, A. Keesling, G. Semeghini, S. Ebadi, T. T. Wang, A. A. Michailidis, N. Maskara, W. W. Ho, S. Choi, M. Serbyn, M. Greiner, V. Vuletić, and M. D. Lukin, "Controlling quantum many-body dynamics in driven Rydberg atom arrays," Science **371**, 1355–1359 (2021).
[40] Dolev Bluvstein, Harry Levine, Giulia Semeghini, Tout T. Wang, Sepehr Ebadi, Marcin Kalinowski, Alexander Keesling, Nishad Maskara, Hannes Pichler, Markus Greiner, Vladan Vuletić, and Mikhail D. Lukin, "A quantum processor based on coherent transport of entangled atom arrays," Nature **604**, 451–456 (2022).
[41] Guo-Xian Su, Hui Sun, Ana Hudomal, Jean-Yves Desaules, Zhao-Yu Zhou, Bing Yang, Jad C. Halimeh, Zhen-Sheng Yuan, Zlatko Papić, and Jian-Wei Pan, "Observation of many-body scarring in a Bose-Hubbard quantum simulator," Phys. Rev. Res. **5**, 023010 (2023).
[42] Pengfei Zhang, Hang Dong, Yu Gao, Liangtian Zhao, Jie Hao, Jean-Yves Desaules, Qiujiang Guo, Jiachen Chen, Jinfeng Deng, Bobo Liu, Wenhui Ren, Yunyan Yao, Xu Zhang, Shibo Xu, Ke Wang, Feitong Jin, Xuhao Zhu, Bing Zhang, Hekang Li, Chao Song, Zhen Wang, Fangli Liu, Zlatko Papić, Lei Ying, H. Wang, and Ying-Cheng Lai, "Many-body Hilbert space scarring on a superconducting processor," Nature Physics **19**, 120–125 (2023).
[43] Hang Dong, Jean-Yves Desaules, Yu Gao, Ning Wang, Zexian Guo, Jiachen Chen, Yiren Zou, Feitong Jin, Xuhao Zhu, Pengfei Zhang, Hekang Li, Zhen Wang, Qiujiang Guo, Junxiang Zhang, Lei Ying, and Zlatko Papić, "Disorder-tunable entanglement at infinite temperature," Science Advances **9**, eadj3822 (2023).
[44] Federica M. Surace, Paolo P. Mazza, Giuliano Giudici, Alessio Lerose, Andrea Gambassi, and Marcello Dalmonte, "Lattice gauge theories and string dynamics in Rydberg atom quantum simulators," Phys. Rev. X **10**, 021041 (2020).
[45] Thomas Iadecola and Michael Schecter, "Quantum many-body scar states with emergent kinetic constraints and finite-entanglement revivals," Phys. Rev. B **101**, 024306 (2020).
[46] Debasish Banerjee and Arnab Sen, "Quantum scars from zero modes in an abelian lattice gauge theory on ladders," Phys. Rev. Lett. **126**, 220601 (2021).
[47] Jad C. Halimeh, Luca Barbiero, Philipp Hauke, Fabian Grusdt, and Annabelle Bohrdt, "Robust quantum many-body scars in lattice gauge theories," Quantum **7**, 1004 (2023).
[48] Ana Hudomal, Jean-Yves Desaules, Bhaskar Mukherjee, Guo-Xian Su, Jad C. Halimeh, and Zlatko Papić, "Driving quantum many-body scars in the PXP model," Phys. Rev. B **106**, 104302 (2022).
[49] Jean-Yves Desaules, Debasish Banerjee, Ana Hudomal, Zlatko Papić, Arnab Sen, and Jad C. Halimeh, "Weak ergodicity breaking in the Schwinger model," Phys. Rev. B **107**, L201105 (2023).
[50] Jean-Yves Desaules, Ana Hudomal, Debasish Banerjee, Arnab Sen, Zlatko Papić, and Jad C. Halimeh, "Prominent quantum many-body scars in a truncated Schwinger model," Phys. Rev. B **107**, 205112 (2023).
[51] Adith Sai Aramthottil, Utso Bhattacharya, Daniel González-Cuadra, Maciej Lewenstein, Luca Barbiero, and Jakub Zakrzewski, "Scar states in deconfined $\mathbb{Z}_2$ lattice gauge theories," Phys. Rev. B **106**, L041101 (2022).
[52] Saptarshi Biswas, Debasish Banerjee, and Arnab Sen, "Scars from protected zero modes and beyond in $U(1)$ quantum link and quantum dimer models," SciPost Phys. **12**, 148 (2022).
[53] Aiden Daniel, Andrew Hallam, Jean-Yves Desaules, Ana Hudomal, Guo-Xian Su, Jad C. Halimeh, and Zlatko Papić, "Bridging quantum criticality via many-body scarring," Phys. Rev. B **107**, 235108 (2023).
[54] Lukas Ebner, Andreas Schäfer, Clemens Seidl, Berndt Müller, and Xiaojun Yao, "Entanglement entropy of (2+1)-dimensional SU(2) lattice gauge theory," arXiv eprints (2024), arXiv:2401.15184 [hep-lat].
[55] Indrajit Sau, Paolo Stornati, Debasish Banerjee, and Arnab Sen, "Sublattice scars and beyond in two-dimensional $U(1)$ quantum link lattice gauge theories," Phys. Rev. D **109**, 034519 (2024).
[56] Jesse Osborne, Ian P. McCulloch, and Jad C. Halimeh, "Quantum many-body scarring in $2+1$D gauge theories with dynamical matter," arXiv eprints (2024), arXiv:2403.08858 [cond-mat.quant-gas].
[57] Thea Budde, Marina Krstić Marinković, and Joao C. Pinto Barros, "Quantum many-body scars for arbitrary integer spin in 2+1D abelian gauge theories," arXiv eprints (2024), arXiv:2403.08892 [hep-lat].
[58] Umberto Borla, Ruben Verresen, Fabian Grusdt, and Sergej Moroz, "Confined phases of one-dimensional spinless fermions coupled to Z_2 gauge theory," Phys. Rev. Lett. **124**, 120503 (2020).
[59] Matja ž Kebrič, Luca Barbiero, Christian Reinmoser, Ulrich Schollwöck, and Fabian Grusdt, "Confinement and Mott transitions of dynamical charges in one-dimensional lattice gauge theories," Phys. Rev. Lett. **127**, 167203 (2021).
[60] Matjaž Kebrič, Umberto Borla, Ulrich Schollwöck, Sergej Moroz, Luca Barbiero, and Fabian Grusdt, "Confinement induced frustration in a one-dimensional $\mathbb{Z}_2$ lattice gauge theory," New Journal of Physics **25**, 013035 (2023).
[61] Lukas Homeier, Annabelle Bohrdt, Simon Linsel, Eugene Demler, Jad C. Halimeh, and Fabian Grusdt, "Realistic scheme for quantum simulation of $\mathbb{Z}_2$ lattice gauge theories with dynamical matter in $(2+1)$D," Communications Physics **6**, 127 (2023).
[62] Simon M. Linsel, Annabelle Bohrdt, Lukas Homeier, Lode Pollet, and Fabian Grusdt, "Percolation as a confinement order parameter in $\mathbb{Z}_2$ lattice gauge theories," arXiv eprints (2024), arXiv:2401.08770 [quant-ph].
[63] Matjaž Kebrič, Jad C. Halimeh, Ulrich Schollwöck, and Fabian Grusdt, "Confinement in 1+1D $\mathbb{Z}_2$ lattice gauge theories at finite temperature," arXiv eprints (2023), arXiv:2308.08592 [cond-mat.quant-gas].
[64] Michael Fromm, Owe Philipsen, Michael Spannowsky, and Christopher Winterowd, "Simulating $\mathbb{Z}_2$ lattice gauge theory with the variational quantum thermalizer," EPJ Quantum Technology **11**, 20 (2024).
[65] See the Supplemental Material for background calculations and additional examples that support the results in the main text. The Supplemental Material contains

Refs. [29, 45, 58, 69, 76, 77, 80, 81].
[66] Zhi-Cheng Yang, Fangli Liu, Alexey V. Gorshkov, and Thomas Iadecola, "Hilbert-space fragmentation from strict confinement," Phys. Rev. Lett. **124**, 207602 (2020).
[67] Sergey Bravyi, David P. DiVincenzo, and Daniel Loss, "Schrieffer–wolff transformation for quantum many-body systems," Annals of Physics **326**, 2793 – 2826 (2011).
[68] Shuichi Inokuchi, "On behaviors of cellular automata with rule 156," Bulletin of Informatics and Cybernetics **30**, 121 – 131 (1998).
[69] Somnath Maity and Ryusuke Hamazaki, "Kinetically constrained models constructed from dissipative quantum dynamics," arXiv e-Prints (2024), arXiv:2403.12548 [quant-ph].
[70] Pablo Sala, Tibor Rakovszky, Ruben Verresen, Michael Knap, and Frank Pollmann, "Ergodicity breaking arising from hilbert space fragmentation in dipole-conserving Hamiltonians," Phys. Rev. X **10**, 011047 (2020).
[71] Vedika Khemani, Michael Hermele, and Rahul Nandkishore, "Localization from Hilbert space shattering: From theory to physical realizations," Phys. Rev. B **101**, 174204 (2020).
[72] S Chandrasekharan and U.-J Wiese, "Quantum link models: A discrete approach to gauge theories," Nuclear Physics B **492**, 455 – 471 (1997).
[73] U.-J. Wiese, "Ultracold quantum gases and lattice systems: quantum simulation of lattice gauge theories," Annalen der Physik **525**, 777–796 (2013).
[74] Jean-Yves Desaules, Guo-Xian Su, Ian P. McCulloch, Bing Yang, Zlatko Papić, and Jad C. Halimeh, "Ergodicity breaking under confinement in cold-atom quantum simulators," Quantum **8**, 1274 (2024).
[75] Alastair Kay, "Perfect, efficient, state transfer and its application as a constructive tool," International Journal of Quantum Information **08**, 641–676 (2010).
[76] Vadim Oganesyan and David A. Huse, "Localization of interacting fermions at high temperature," Phys. Rev. B **75**, 155111 (2007).
[77] Y. Y. Atas, E. Bogomolny, O. Giraud, and G. Roux, "Distribution of the ratio of consecutive level spacings in random matrix ensembles," Phys. Rev. Lett. **110**, 084101 (2013).
[78] Jean-Yves Desaules, Ana Hudomal, Christopher J. Turner, and Zlatko Papić, "Proposal for realizing quantum scars in the tilted 1D Fermi-Hubbard model," Phys. Rev. Lett. **126**, 210601 (2021).
[79] Alvise Bastianello, Umberto Borla, and Sergej Moroz, "Fragmentation and emergent integrable transport in the weakly tilted Ising chain," Phys. Rev. Lett. **128**, 196601 (2022).
[80] Brian J. J. Khor, D. M. Kurkcuoglu, T. J. Hobbs, G. N. Perdue, and Israel Klich, "Confinement and kink entanglement asymmetry on a quantum Ising chain," arXiv preprint (2023), arXiv:2312.08601.
[81] Igor Lesanovsky and Hosho Katsura, "Interacting Fibonacci anyons in a Rydberg gas," Phys. Rev. A **86**, 041601 (2012).

Supplemental Online Material for "Mass-Assisted Local Deconfinement in a Confined $\mathbb{Z}_2$ Lattice Gauge Theory"

Jean-Yves Desaules[1], Thomas Iadecola[2,3], and Jad C. Halimeh[4,5,6]

[1] *Institute of Science and Technology Austria (ISTA), Am Campus 1, 3400 Klosterneuburg, Austria*

[2] *Department of Physics and Astronomy, Iowa State University, Ames, IA 50011, USA*

[3] *Ames National Laboratory, Ames, IA 50011, USA*

[4] *Department of Physics and Arnold Sommerfeld Center for Theoretical Physics (ASC), Ludwig-Maximilians-Universität München, Theresienstraße 37, D-80333 München, Germany*

[5] *Munich Center for Quantum Science and Technology (MCQST), Schellingstraße 4, D-80799 München, Germany*

[6] *Dahlem Center for Complex Quantum Systems, Freie Universität Berlin, 14195 Berlin, Germany*

In this Supplemental Material, we provide additional analysis supporting the results in the main text. In Sec. I, we review the symmetries of the model and show that it is chaotic. In Sec. II, we give additional details on the mapping to the $\mathbb{Z}_2$ LGT. In Sec. III, we show that the exact scars that were found in Ref. [45] are also present in this model but do not contribute to the dynamics we see. In Sec. IV, we provide additional details and derivations regarding the properties of the Hamiltonian $\hat{H}_{\text{eff}}$. In Sec. V, we explore the consequences of detuning between μ and h. In Sec. VI, we give additional data on the overlap of the initial states studied in the main text with the eigenstates. In Sec. VII, we perform a detailed analysis of the origin of scarring in $\hat{H}_{\text{eff}} + \hat{H}^{(2)}_{\text{eff}}$. In Sec. VIII, we study the optimal deformation $|\Psi_2'\rangle$ of $|\Psi_2\rangle$ to maximize the revival fidelity. In Sec. IX, we show the effective Hamiltonian at third order and briefly discuss its effects. Finally, in Sec. X we discuss the dynamics in terms of the fermionic degrees of freedom.

I. MODEL AND SYMMETRIES

In this section we review the properties of the Hamiltonian that we study in the main text, as defined in Eq. (1), and show that it is chaotic. This Hamiltonian conserves the number of domain walls,

$$\hat{N}_{\text{DW}} = \sum_j \frac{1 - \hat{Z}_j \hat{Z}_{j+1}}{2}. \tag{S1}$$

This splits the system into $L/2$ sectors for L even and with periodic boundary conditions (PBC). In addition, for even L the system is also invariant under spatial reflection and translation by two sites. We observe that applying a translation by a single site maps to the same model but with $\mu \to -\mu$. In a similar way, performing a particle-hole exchange $\sum_j \hat{X}_j$ only changes h to $-h$ while leaving the other parameters invariant. This means that we can focus solely on the case where $\mu, h \geq 0$, as the other three sectors are identical up to a unitary transformation.

To verify that the Hamiltonian is chaotic, we check the energy level statistics, and in particular the mean energy spacing ratio [76]. This is plotted in Fig. S1(a) and shows $\langle r \rangle \approx 0.53$ in a relatively broad range of parameters. This is the value expected from the Wigner-Dyson distribution which is relevant for a real-valued random matrix [77]. For $\mu = 0$ the model has additional symmetries (translation by one instead of two sites) while for $h = 0$ the model is integrable via a mapping to free fermions [45, 80]. Along the resonant regime $\mu = h$ that we explore in the main text, the level spacing statistics indicate that the model is chaotic until $\mu = h \approx J$ for $L = 20$, as shown in Fig. S1(b). Additionally, we check the full distribution of level spacings for incommensurate values of h and μ in Fig. S1(c), once again finding good agreement with the Wigner-Dyson distribution.

II. MAPPING TO THE $\mathbb{Z}_2$ LATTICE GAUGE THEORY

The model we consider in the main text maps exactly to the $1+1$D $\mathbb{Z}_2$ LGT with Hamiltonian [58]

$$\hat{H} = \sum_j \Big[J\big(\hat{c}_j^\dagger \hat{c}_{j+1} + \text{H.c.}\big)\hat{\tau}^z_{j,j+1} + h\hat{\tau}^x_{j,j+1} + \mu(-1)^j \hat{n}_j \Big], \tag{S2}$$

where $\hat{c}_j^\dagger / \hat{c}_j$ create/annihilate a fermion on site j and $\hat{n}_j = \hat{c}_j^\dagger \hat{c}_j$ is the fermion density. The Pauli operators $\hat{\tau}^z_{j,j+1}$ and $\hat{\tau}^x_{j,j+1}$ represent the local gauge and electric fields at the link between the two neighboring sites j and $j+1$, h is the electric-field strength, and μ is the mass. The generator of the $\mathbb{Z}_2$ gauge symmetry is

$$\hat{G}_j = -(-1)^{\hat{n}_j} \hat{\tau}^x_{j-1,j} \hat{\tau}^x_{j,j+1}, \tag{S3}$$

which has two eigenvalues $g_j = \pm 1$, so-called *background charges*.

Within the gauge-invariant sector $\{|\Psi\rangle\}$ satisfying $\hat{G}_j |\Psi\rangle = |\Psi\rangle, \forall j$, Eq. (S2) can be expressed as the Ising spin Hamiltonian that we use in the main text [58], as defined in Eq. (1). The $\mathbb{Z}_2$ gauge variables are $\hat{\tau}^z_{j,j+1} \equiv \hat{X}_j$ and $\hat{\tau}^x_{j,j+1} \equiv \hat{Z}_j$, while the gauge-invariant fermion density $\hat{n}_j \equiv (1 - \hat{Z}_j \hat{Z}_{j+1})/2$. Thus, in the spin-1/2 Hamiltonian, the fermions are represented by domain walls between up and down spins, and fermion number conservation is manifested as conservation of the domain wall number $\hat{N}_{\text{DW}} = \sum_j \hat{n}_j$.

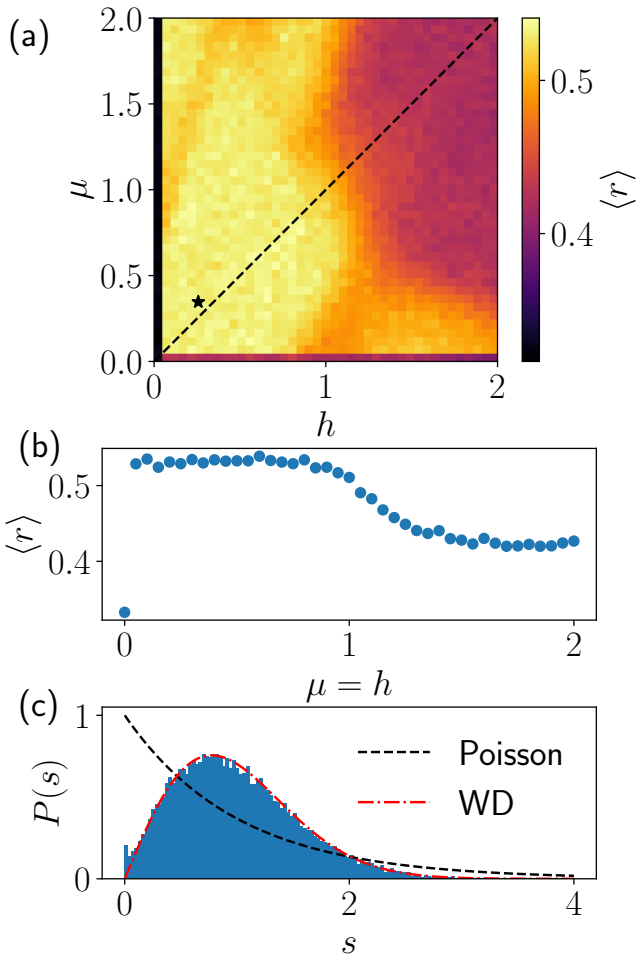

FIG. S1. Level spacing statistics in the sector with $2\lfloor L/4 \rfloor$ domain walls, zero momentum, and eigenvalue $+1$ under spatial reflection. (a) Mean level spacing ratio [76] for a wide range of values of μ and h for $L = 20$. In a broad range of values, we have $\langle r \rangle \approx 0.53$, as expected for a chaotic system [77]. The dashed line indicates $\mu = h$, for which the data is plotted in panel (b). The black star indicates the parameter used in panel (c). (b) Mean level spacing ratio for $\mu = h$ for $L = 20$. The system is chaotic until around $\mu = h = 1$. (c) Full distribution of level spacings after unfolding for $L = 22$ with $\mu = \sqrt{3}/5 \approx 0.346$ and $h = \sqrt{8}/11 \approx 0.257$. There is clear agreement with the Wigner-Dyson distribution for the Gaussian orthogonal ensemble, indicating that the model is chaotic.

III. EXACT QUANTUM MANY-BODY SCARS

In this section, we discuss the presence of exact quantum many-body scars (QMBSs) in the model. If we consider the same model as in the main text but without the staggering in the ZZ term, then it has been shown to hosts two families of exact QMBS [45]. When the ZZ term is staggered, the same states are still present, as shown in Fig. S2. However, their energy now only depends on the field h and not on μ, as $E_n = h(-L + 2n)$ with $n = 0$ to $L + 1$. Indeed, scarred eigenstates of the first kind are symmetric superpositions of all Fock states with a fixed number of up-spins but none of them next to each other. These isolated up-spins do not change the energy of the mass term, as they create two domain walls but on even-odd and odd-even sites. Thus their contribution will cancel each other due to the staggering. The second family of scarred states is the same up to a global spin flip. This means that they are symmetric superpositions of all Fock states with a fixed number of down-spins but none of them next to each other. The same argument holds as to why their energy only depends on h.

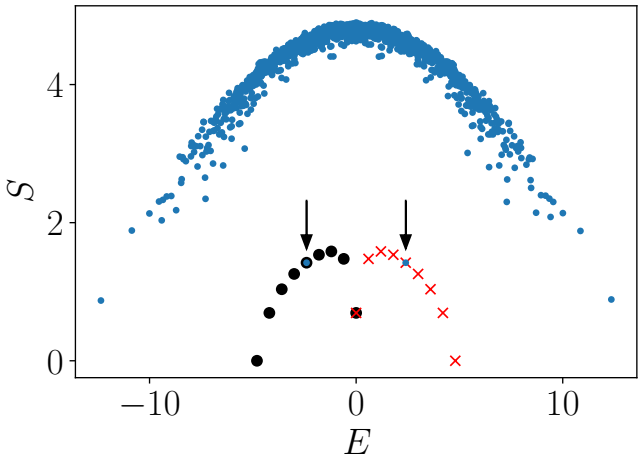

FIG. S2. Entanglement entropy of eigenstates for a chain with 16 sites. The parameters used are $h = 0.3$ and $\mu = 0.74$. The blue dots are eigenstates in the sector with 8 domain walls, zero momentum, and eigenvalue $+1$ under spatial inversion. The black and red markers indicates the two families of exact scars found in Ref. [45], which have an energy spacing of $2h$. The arrows highlight which states among them live in the same symmetry sector as the rest of the data.

Importantly, these $N + 1$ scarred states are all eigenstates of $\hat{H}_0$. This means that they will not get split up into different eigenstates as $\mu = h$ is increased. Instead, they will be exact eigenstates of *all* the higher order Schrieffer-Wolff terms independently. Nonetheless, we emphasize that they do not contribute at all to the scarring we observe from the $|\Phi\rangle$ and $|\Psi_2\rangle$ states. First of all, as both of these states have a definite number of up-spins they could have overlap with at most one of the exact scarred states. Thus, the equal spacing with the other QMBSs would be irrelevant for the dynamics. On top of that, we can show that these QMBSs have exactly zero overlap with $|\Psi_2\rangle$ and $|\Phi\rangle$. For the former this is easy to see, as $|\Psi_2\rangle$ has both consecutive down-spins and consecutive up-spins. For the latter, we need to take into the account the phases in the states composing the exact QMBSs. Having an up-spin on an odd site leads to a phase factor of -1 while it is $+1$ if the up-spin is on an even site. So we can write the relevant part of the scarred state as a tensor product of 4-site cells where each cell is

$(|{\downarrow}{\uparrow}{\downarrow}{\downarrow}\rangle - |{\downarrow}{\downarrow}{\uparrow}{\downarrow}\rangle)/\sqrt{2}$. As for the $|\Phi\rangle$ state, each cell is in the state $(|{\downarrow}{\uparrow}{\downarrow}{\downarrow}\rangle + |{\downarrow}{\downarrow}{\uparrow}{\downarrow}\rangle)/\sqrt{2}$, and we immediately see that they are orthogonal.

IV. PROPERTIES OF $\hat{H}_{\text{eff}}$

In this section we provide additional information and examples regarding the structure of

$$\hat{H}_{\text{eff}} = J \sum_{j \text{ odd}} \hat{Q}_{j-1}\hat{X}_j\hat{P}_{j+1} + J \sum_{j \text{ even}} \hat{P}_{j-1}\hat{X}_j\hat{Q}_{j+1}. \quad \text{(S4)}$$

We recall that this Hamiltonian can be mapped to the "PXQ" model discussed in Ref. [69] which briefly discusses some of its properties such as fragmentation. Here, we review these properties for our model and in the context of LGT. We also derive new properties of the model such as the number of disconnected sectors.

First of all, we briefly show that the operators $\hat{O}_j$ defined as

$$\hat{O}_j = \begin{cases} \hat{Q}_j\hat{Q}_{j+1}, & \text{for } j \text{ odd} \\ \hat{P}_j\hat{P}_{j+1}, & \text{for } j \text{ even} \end{cases} \quad \text{(S5)}$$

do commute with the Hamiltonian. Let us first focus on an odd site j for which $\hat{O}_j = \hat{Q}_j\hat{Q}_{j+1}$. Then the two operators in $\hat{H}_{\text{eff}}$ that can change the value of spins j or $j+1$ are $\hat{Q}_{j-1}\hat{X}_j\hat{P}_{j+1}$ and $\hat{P}_j\hat{X}_{j+1}\hat{Q}_{j+2}$. But as there is always a term $\hat{Q}_j\hat{P}_j = 0$ or $\hat{Q}_{j+1}\hat{P}_{j+1}$, they get annihilated by $\hat{O}_j$. The exact same can be done with even sites for which $\hat{O}_j = \hat{P}_j\hat{P}_{j+1}$—there, the two terms of $\hat{H}_{\text{eff}}$ that can modify sites j or $j+1$ are $\hat{P}_{j-1}\hat{X}_j\hat{Q}_{j+1}$ and $\hat{Q}_j\hat{X}_{j+1}\hat{P}_{j+2}$. So $\hat{H}_{\text{eff}}$ commutes with all $\hat{O}_j$ and almost all Krylov subspaces can be identified through the expectation values of these operators.

The only constraint on the O_j is that O_j and O_{j+1} cannot both be one at the same time. Indeed, the first one includes $\hat{Q}_{j+1}$ while the second includes $\hat{P}_{j+1}$ (or the opposite depending on the parity on j). Thus the number of possible configurations of the O_j is equivalent to the number of states in the PXP model [81] with L sites, plus one because of the two Néel states being disconnected. Using the analytical formula from Ref. [29] we arrive at a total of $\mathcal{F}_{L-1} + \mathcal{F}_{L+1} + 1$ sectors, where $\mathcal{F}_n$ is the n-th Fibonacci number.

As mentioned in the main text, between two frozen blocks $O_k = O_{k+r} = 1$ with $O_j = 0$ for $k < j < k+r$, the effective model is that of a tight-binding chain. On top of this, the effective particle that hops in the chain corresponds to a hole on top of a background of matter in the LGT picture. While this is not very intuitive, we can provide an illustrative example. Let us consider the state $|{\uparrow}{\uparrow}{\uparrow}{\downarrow}{\uparrow}{\downarrow}{\uparrow}{\downarrow}{\uparrow}{\uparrow}\cdots\rangle$. We can check that $O_1 = O_9 = 1$ and that all the O_j in between are equal to 0. All possible configurations are shown in Fig. S3(a), and it is straightforward to count that there are $7 = 8-1$ of them and that they form an effective tight-binding chain. In Fig. S3(b), we also show the matter configurations corresponding to the same states. It immediately becomes apparent that the effective particle hopping in the tight-binding chain is a hole on top of a fully packed matter background.

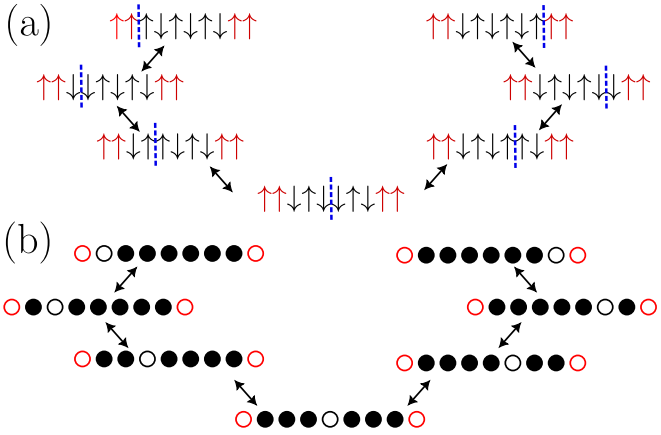

FIG. S3. (a) Example of the possible configurations in a part of the chain between two frozen domains. Frozen sites are highlighted in red, while the blue dashed line indicates the boundary between two inequivalent Néel domains. This boundary can move, and the effective dynamics in that part of the chain is that of a tight-binding chain with a single particle. (b) Matter configurations corresponding to the gauge configurations in (a), making apparent the nature of the particle hopping in the tight-binding chain. It corresponds to a hole on top of a fully packed background of matter.

V. DETUNING

In this section, we consider the case where h and μ are not exactly equal. In particular, we will set $h = \mu + \delta$ where δ is the detuning. As long as δ is small compared to h and μ, we can perform the Schrieffer-Wolff transformation with the same $\hat{H}_0$ where $h = \mu$, but with an additional term $\delta \sum_j \hat{Z}_j$ in $\hat{V}$. This additional term will directly appear in $\hat{H}_{\text{eff}}$ at order 1. It will not influence the terms at second order but will have an effect at third order. Indeed, there will be new terms appearing at third order with a prefactor of $J^2\delta/\mu^2$. These new terms can actually be simply described as $-\frac{\delta}{2\mu}\hat{H}^{(2)}_{\text{eff}}$, as they correspond to inserting the diagonal field δ in the process described by $\hat{H}^{(2)}_{\text{eff}}$.

If we only look at the first order term, since the detuning term is a simple Z-field it will not change the connectivity. So the Hilbert space fragmentation is not affected. In each disconnected part of the chain, moving the hole is done by flipping a spin up or down depending on the parity of the site. This means that the effective particle will feel a staggered Z-field. Since this just adds local Z-terms, it does not kill the mapping to free-fermions and each part of the chain remains integrable.

We can also focus on the effective spin-1 sector. Let us ignore the action of the higher-order Schrieffer-Wolff terms for the moment. In that case, the Z-field will change the effective Hamiltonian of each spin-1 as

$$\begin{pmatrix} 0 & J & 0 \\ J & 0 & J \\ 0 & J & 0 \end{pmatrix} \rightarrow \begin{pmatrix} -2\delta & J & 0 \\ J & 0 & J \\ 0 & J & -2\delta \end{pmatrix}, \tag{S6}$$

so that the eigenvalues then go from $-\sqrt{2}|J|$, 0 and $\sqrt{2}|J|$ to $-\delta - \sqrt{2J^2+\delta^2}$, -2δ and $-\delta + \sqrt{2J^2+\delta^2}$. This has important consequences. If we quench from $|\Psi_2\rangle$, then only the highest and lowest eigenvalues are involved. This means that there is a single energy spacing of $2\sqrt{2J^2+\delta^2}$ so that revivals still occur but with a renormalized period of $\pi/\sqrt{2J^2+\delta^2}$. Meanwhile, if we quench from $|\Psi_4\rangle$ then all three eigenvalues are involved and we get two different energy spacings. We can only get perfect revivals if these are commensurate, meaning if $\delta + \sqrt{2J^2+\delta^2} = n\left(\sqrt{2J^2+\delta^2} - \delta\right)$, with n a rational number. We can turn that expression into $\delta = \pm\frac{(n-1)|J|}{\sqrt{2n}}$. For n integer, the revival then has a period of $(n+1)\pi/\sqrt{2J^2+\delta^2}$. The case with no detuning corresponds to $n=1$ and we recover that $|\Psi_4\rangle$ revives with twice the period of $|\Psi_2\rangle$. This dependence on detuning is shown in Fig. S4 for various integer n.

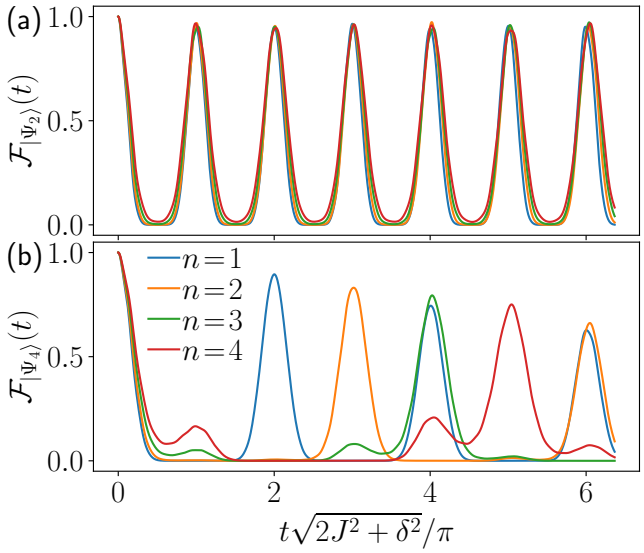

FIG. S4. Fidelity after a quench from the states $|\Psi_2\rangle$ (top) and $|\Psi_4\rangle$ (bottom) with $L=16$ and $\mu=5$. Each curve corresponds to a different detuning $\frac{(n-1)}{\sqrt{2n}}$. For $|\Psi_2\rangle$, only the period and fidelity minimum changes with detuning. Meanwhile, for $|\Psi_4\rangle$ the period is directly affected by detuning.

We can also ask if there is any interesting interaction between the higher order Schrieffer-Wolff terms and the detuning. Interestingly, in each spin-1 cell the effect of the detuning is the opposite of that of the diagonal part of $\hat{H}^{(2)}_{\text{eff}}$. Indeed, the action of the latter in the spin-1 sector is

$$\begin{pmatrix} 0 & J & 0 \\ J & 0 & J \\ 0 & J & 0 \end{pmatrix} \rightarrow \begin{pmatrix} -1/(4\mu) & J & 0 \\ J & -1/(2\mu) & J \\ 0 & J & -1/(4\mu) \end{pmatrix}. \tag{S7}$$

Looking at both (S7) and Eq. (S6), if we combine their action we get that the diagonal term becomes $-2\delta - 1/(4\mu)$, $-1/(2\mu)$ and $-2\delta - 1/(4\mu)$. Choosing $\delta = 1/(8\mu)$ makes all these terms equal to $-1/(2\mu)$ and so restores the equal spacing of the three energy levels. For added accuracy, we can also consider the effect of the third order term. With detuning, its diagonal contribution is equal to $-\frac{\delta}{2\mu}$ times that of $\hat{H}^{(2)}_{\text{eff}}$. This means we can just multiply the diagonal term of $\hat{H}^{(2)}_{\text{eff}}$ by a factor of $1-\delta/(2\mu)$. This changes the optimal δ from $\frac{1}{8\mu}$ to $\frac{1}{8\mu}\frac{1}{1+1/(16\mu^2)}$. While adding this detuning has little effect on revivals from $|\Psi_2\rangle$, it actually improves revivals from $|\Psi_4\rangle$. This is shown in Fig. S5. The effect is visible but small, as most of the revival decay is caused by leakage which is not corrected by the detuning.

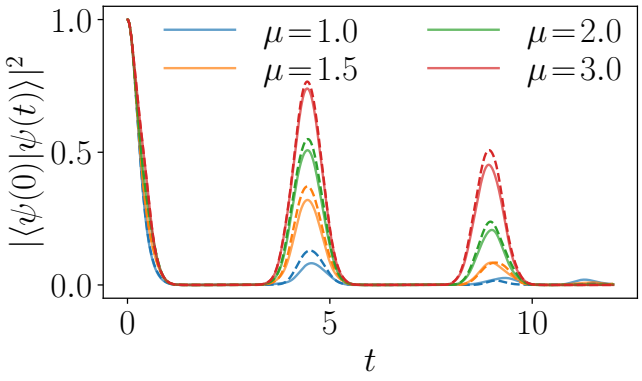

FIG. S5. Fidelity after a quench from the $|\Psi_4\rangle$ with $L=16$ close to the resonant point $\mu=h$. Each color corresponds to a different value of μ. Solid curves are with no detuning while dashed lines are with $\delta = \frac{1}{8\mu}\frac{1}{1+1/(16\mu^2)}$. While the effect is small, the latter consistently shows better revivals.

VI. OVERLAP OF EIGENSTATES WITH CDW STATES

In the main text, we show the overlap of the $|\Phi\rangle$ state with the eigenstates. In this Section, we show the same data for the other initial states as well as for various values of μ. Figs. S6, S7 and S8 show the eigenstate overlaps of the $|\Phi\rangle$, $|\Psi_2\rangle$ and $|\Psi_4\rangle$ states for $\mu = h = 0.8$, 1.5 and 3.

As expected, the presence of revivals for a state at a given value of μ correlates with the presence of eigenstates with predominant overlap. We can further verify that these states match with the spin-1 predictions. The energy spacing of the scarred states should then be

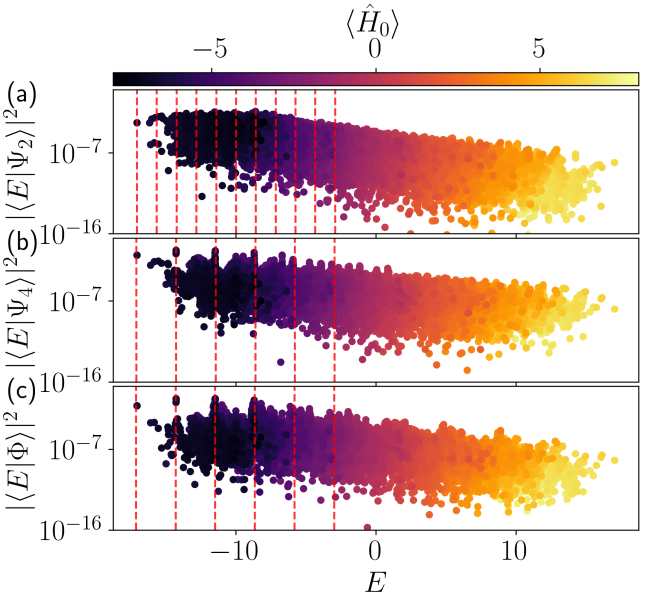

FIG. S6. Overlap of the $|\Psi_2\rangle$, $|\Psi_4\rangle$ and $|\Phi\rangle$ states with the eigenstates of the Hamiltonian for $L = 20$ and $\mu = h = 0.8$. The color indicates the expectation value of $\hat{H}_0$ with respect to each eigenstate. The red dashed lines are spaced in energy according to the spin-1 predictions and are aligned with the eigenstate with the highest overlap.

$\Delta E = 2J$ for $|\Psi_4\rangle$ and $\Delta E = \sqrt{8}J$ for $|\Psi_2\rangle$ and $|\Phi\rangle$. Additionally, they should be centered around $-\mu L/2$, which is the expectation of $\hat{H}_0$ is their sector. However, due to interactions with the other sectors we find that this is always shifted towards higher energies for finite $\mu = h$. Nonetheless, the energy spacing inside the sector matches well with the spin-1 picture. In Figs. S6-S8, the red dashed lines have the expected spin-1 energy spacing and are aligned such that the eigenstate with the highest overlap is exactly on a dashed line. We find that the other scarred eigenstates occur at the same energies as the other dashed lines, indicating the correct energy spacing.

For $|\Phi\rangle$ and $|\Psi_2\rangle$, these structures are also present for $\mu = h = 0.8$, when the sectors of $\hat{H}_0$ are not well separated (see Fig. S6). However, the structures are much more prominent in the lower-energy part of the sector. This is very likely because there is no $\hat{H}_0$ sector at lower energy to merge with. This is not the case for $|\Psi_3\rangle$, for which the overlap with the eigenstates is shown in Fig. S9.

In that figure, we have rescaled the energies by μ in order to compare different values of μ with a similar scale. We note that as Figs. S6-S8 are each for a unique value of μ, doing the same rescaling would affect their panels in the same way and would simply amount to a global change of the X axis. What is important to note in Fig. S9 is that the sector containing the $|\Psi_3\rangle$ state merges with other sectors from *both* sides. For $\mu = 0.8$, that sector is already merging with the neighboring sectors at the energy of all scarred eigenstates except the middle one. This is likely why this state shows less robust revivals than $|\Phi\rangle$ and $|\Psi_2\rangle$ for small values of $\mu = h$ despite not being affected by $\hat{H}^{(2)}_{\text{eff}}$.

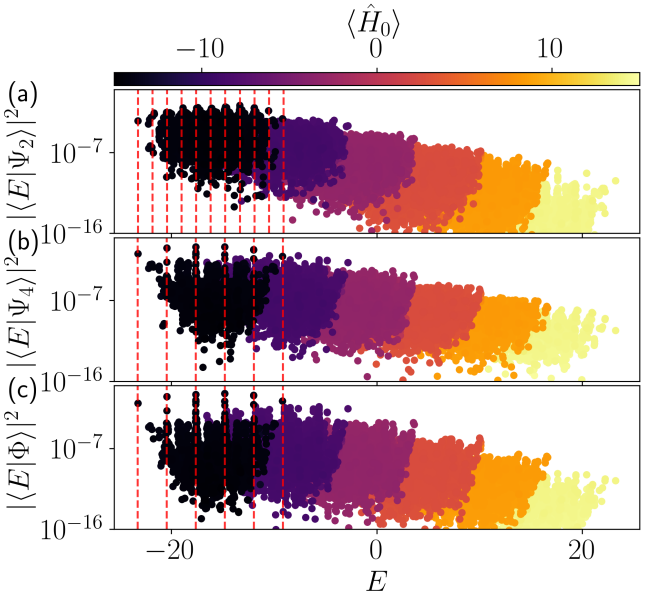

FIG. S7. Overlap of the $|\Psi_2\rangle$, $|\Psi_4\rangle$ and $|\Phi\rangle$ states with the eigenstates of the Hamiltonian for $L = 20$ and $\mu = h = 1.5$. The color indicates the expectation value of $\hat{H}_0$ with respect to each eigenstate. The red dashed lines are spaced in energy according to the spin-1 predictions and are aligned with the eigenstate with the highest overlap.

VII. DYNAMICS AT FIRST AND SECOND ORDERS

In this section, we investigate the properties of the Hamiltonian $\hat{H}' = \hat{H}_{\text{eff}} + \hat{H}^{(2)}_{\text{eff}}$. We recall that

$$H^{(2)}_{\text{eff}} = \frac{J^2}{4\mu}\Big[\sum_{j \text{ even}} \hat{Q}_{j-1}(\hat{\sigma}^+_j\hat{\sigma}^-_{j+1} + \hat{\sigma}^-_j\hat{\sigma}^+_{j+1})\hat{Q}_{j+2} - \sum_{j \text{ odd}} \hat{P}_{j-1}(\hat{\sigma}^+_j\hat{\sigma}^-_{j+1} + \hat{\sigma}^-_j\hat{\sigma}^+_{j+1})\hat{P}_{j+2} + \sum_{j \text{ even}} \hat{Q}_{j-1}\hat{Z}_j\hat{P}_{j+1} + \sum_{j \text{ odd}} \hat{P}_{j-1}\hat{Z}_j\hat{Q}_{j+1}\Big], \tag{S8}$$

while $\hat{H}_{\text{eff}}$ is given in Eq. S4.

We can first look at the effect of $\hat{H}^{(2)}_{\text{eff}}$ on $|\Psi_3\rangle$. Due to the frozen blocks alternating between $\uparrow\uparrow$ and $\downarrow\downarrow$, the dynamical terms are always annihilated and $\hat{H}^{(2)}_{\text{eff}}$ does not create leakage out of the spin-1/2 subspace. So for system sizes that are multiples of 6 and in sectors with $L/3$ domain walls, the Hilbert space admits three isolated spin-1/2 sectors of dimension $2^{L/3}$ which are related by

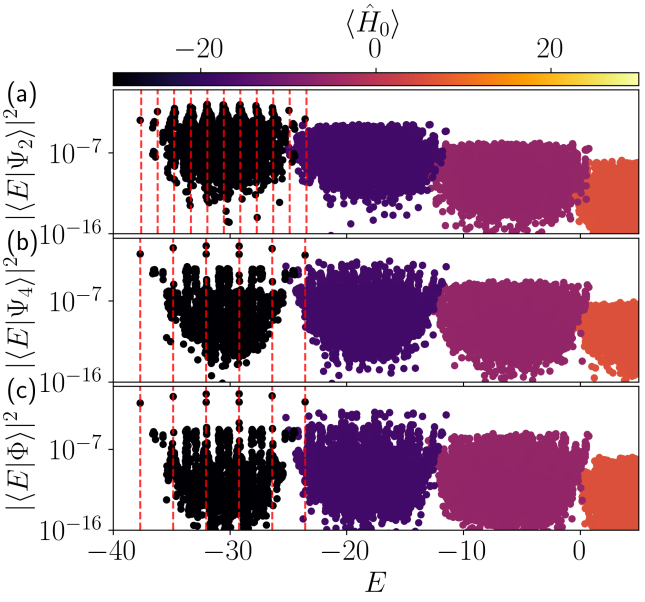

FIG. S8. Overlap of the $|\Psi_2\rangle$, $|\Psi_4\rangle$ and $|\Phi\rangle$ states with the eigenstates of the Hamiltonian for $L = 20$ and $\mu = h = 3$. The color indicates the expectation value of $\hat{H}_0$ with respect to each eigenstate. The red dashed lines are spaced in energy according to the spin-1 predictions and are aligned with the eigenstate with the highest overlap.

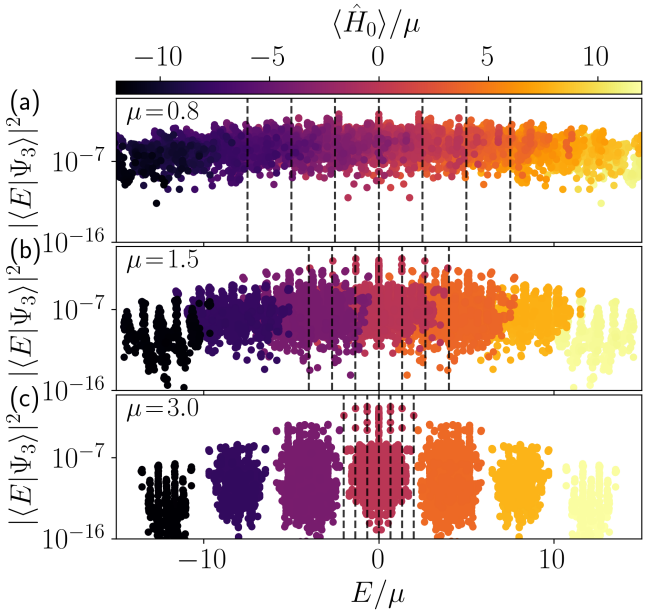

FIG. S9. Overlap of $|\Psi_3\rangle$ with the eigenstates of the Hamiltonian for $L = 20$ and $\mu = h = 0.8$, 1.5 and 3. The color indicates the expectation value of $\hat{H}_0/\mu$ with respect to each eigenstate. The black dashed lines denote the exact energies at which the scarred eigenstates are expected according to the spin-1 picture.

two-site translation. In addition, while the diagonal term of $\hat{H}^{(2)}_{\text{eff}}$ is not constant in the spin-1/2 subspace, it is always equal to zero along the dynamical trajectory of $|\Psi_3\rangle$. This is because unfrozen spins on odd sites are always in the opposite state as unfrozen spins on even sites. When an even site j is $\downarrow$, this allows the term $\hat{P}_j\hat{Z}_{j+1}\hat{Q}_{j+2}$ to be $+1$. But at the same time, the odd site $k = j + 3$ is $\uparrow$, allowing $\hat{Q}_k\hat{Z}_{k+1}\hat{P}_{k+2}$ to be -1. The same can be seen when j is $\uparrow$ and k is $\downarrow$, but with the terms $\hat{P}_{j-1}\hat{Z}_{j-1}\hat{Q}_j$ and $\hat{Q}_{k-2}\hat{Z}_{k-1}\hat{P}_k$. Thus we find that $\hat{H}^{(2)}_{\text{eff}}$ has absolutely no impact on the revivals of the $|\Psi_3\rangle$ state, which explains why the revivals are not destroyed for values of $\mu = h$ of order 1, unlike for $|\Psi_4\rangle$.

For the $(\hat{N}_{\text{DW}}, \hat{H}_0)$ sector containing $|\Psi_2\rangle$, $|\Psi_4\rangle$ and $|\Phi\rangle$, we will first show that the Hamiltonian $\hat{H}'_{\text{eff}}$ is chaotic. To demonstrate this, we again compute the level statistics, as shown in Fig. S10. The results show good agreement with the Wigner-Dyson distribution in a wide range of values of μ. We also check that $\hat{H}'$ has QMBS by checking the dynamics after quenches and the overlap with the states of interest. This is shown in Fig. S11 and we find clear indications of scarring in both the dynamics and overlaps.

Now that we have shown that $\hat{H}'$ is chaotic, scarred, and behaves similarly to the full Hamiltonian, we can start looking into the origin of the scarring. We find that when starting from the $|\Psi_2\rangle$ or $|\Psi_4\rangle$ state, for large enough values of μ the wave function does not spread into the full connected Hilbert space but is limited to

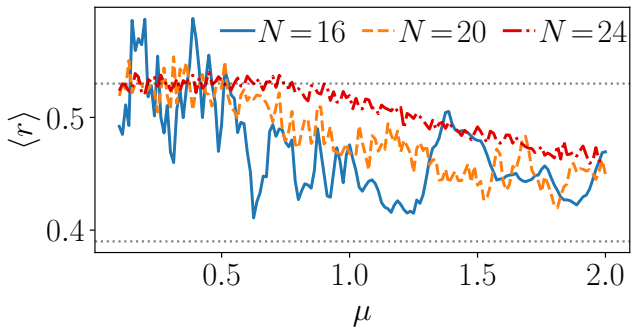

FIG. S10. Mean level spacing ratio of $\hat{H}_{\text{eff}} + \hat{H}^{(2)}_{\text{eff}}$ for various values of $h = \mu$ and various system sizes. All the data are for the symmetry sector containing $|\Psi_2\rangle$, $|\Phi\rangle$ and $|\Psi_4\rangle$, with zero momentum and symmetric under spatial inversion. The dotted lines are at $\langle r \rangle = 0.53$ and $\langle r \rangle = 0.39$, which correspond to respectively Wigner-Dyson for the Gaussian orthogonal ensemble (GOE) and Poisson distribution. For smaller values of μ, there is a good agreement of the data with the GOE result, indicative of a chaotic Hamiltonian.

the spin-1 sector and to the Krylov subspaces of $\hat{H}_{\text{eff}}$ reachable from that sector with a *single* application of $\hat{H}^{(2)}_{\text{eff}}$. We call the latter category "neighbor states." The off-diagonal terms of $\hat{H}^{(2)}_{\text{eff}}$ can only act if a spin-1 cell is in a state $\downarrow\uparrow\downarrow\downarrow$ or $\downarrow\downarrow\uparrow\downarrow$, turning it into $\uparrow\downarrow\downarrow\downarrow$ and $\downarrow\downarrow\downarrow\uparrow$ respectively. Let us look at an 8-site example starting from $|\downarrow\downarrow\uparrow\downarrow\downarrow\downarrow\uparrow\downarrow\rangle$, where the red spins are frozen for $\hat{H}_{\text{eff}}$.

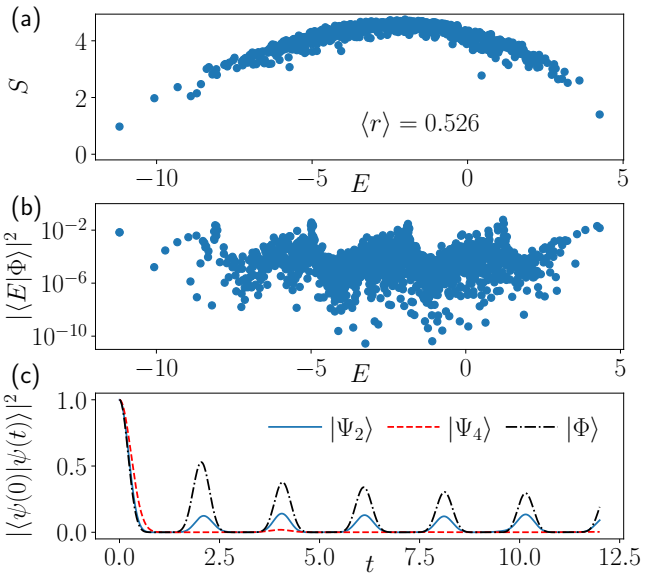

FIG. S11. Properties of $\hat{H}_{\text{eff}} + \hat{H}^{(2)}_{\text{eff}}$ for $\mu = h = 0.5$ and $L = 20$. The entanglement entropy and mean level spacing value in panel (a) are for the symmetry sector with zero momentum and symmetric under spatial reflection. The entanglement entropy of eigenstates is seemingly thermal while the spectrum still holds some nontrivial structure as indicated in the overlap with the $|\Phi\rangle$ state in panel (b). The approximately equal peaks lead to the revivals observed in panel (c).

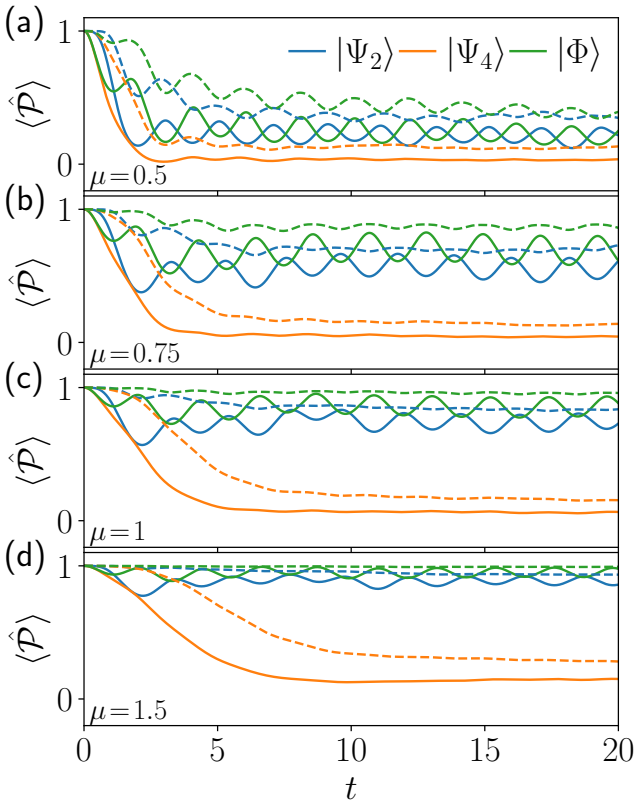

FIG. S12. Dynamics of $\hat{H}_{\text{eff}} + \hat{H}^{(2)}_{\text{eff}}$ for various values of $\mu = h$ after a quench from three different states for $L = 20$. The solid lines show the expectation value of the projector $\hat{\mathcal{P}}_1$ onto the spin-1 subspace, while the dashed lines show the expectation value of the projector $\hat{\mathcal{P}}_2$ onto the spin-1 subspace plus the "neighbor states".

A single application of $\hat{H}^{(2)}_{\text{eff}}$ leads to a superposition of $|{\downarrow}{\downarrow}{\downarrow}\uparrow{\downarrow}{\downarrow}\uparrow{\downarrow}\rangle$ and $|{\downarrow}{\downarrow}\uparrow{\downarrow}{\downarrow}{\downarrow}{\downarrow}\uparrow\rangle$. Effectively, the number of frozen sites is the same, but instead of all free domains having three allowed states we now have one of them with a single state and another with five. This is also true for larger systems. Importantly, applying $\hat{H}^{(2)}_{\text{eff}}$ to a different cell leads to a different Krylov sector of $\hat{H}_{\text{eff}}$, and so there can be no interference between them.

Now that we know what these new sectors look like, we can look at how much of the wave function is contained in them. Fig. S12 shows that after a quench from $|\Psi_2\rangle$ or $|\Phi\rangle$, the wave function is predominantly confined to the spin-1 sector and the "neighbor states" already for $\mu \approx 0.75$. From that figure, it is also very clear that the same is not true for the $|\Psi_4\rangle$ initial state. When starting from it, the fraction of the wave function in the spin-1 sector and in the "neighbor states" sector is essentially unchanged as long as μ is not much greater that J. To understand why this specific phenomenon happens, we have to look at the wave function trajectory once it leaves the spin-1 sector. To do that, we can look at the population of individual states in the "neighbor states" after a quench from $|\Phi\rangle$. This is shown for one Krylov sector of $\hat{H}_{\text{eff}}$ in Fig. S13, and it is clear that the wave function only has significant overlap with a single state. This state is $|{\downarrow}\uparrow\uparrow{\downarrow}\cdots{\downarrow}\uparrow\uparrow{\downarrow}{\downarrow}{\downarrow}{\downarrow}\uparrow{\downarrow}\uparrow\uparrow{\downarrow}\rangle$, and the same state up to translation by two sites and spatial inversion is also dominant in every other sector. We can thus define the state $|\beta\rangle$ as the fully symmetric superposition of these $L/2$ states.

We can now ask why the wave function does not spread further into the "neighbor states". For that, we focus on the simpler case $L = 8$. This is also representative of larger system sizes, as $\hat{H}^{(2)}_{\text{eff}}$ only affects two neighboring cells while the others stay as effective spins-1. In Fig. S14(a), we plot the graph representing the Hamiltonian action in the Hilbert space limited to the Krylov subspaces of interest. For simplicity, we only consider the off-diagonal parts of $\hat{H}^{(2)}_{\text{eff}}$. As the graph has a very regular structure, destructive interference of transition amplitudes can lead to eigenstates with zero overlap on certain Fock states. For example, for all values of μ there is a zero mode (i.e., a state annihilated by the of-diagonal part of $\hat{H}' = \hat{H}_{\text{eff}} + \hat{H}^{(2)}_{\text{eff}}$) comprised only of the $|\beta\rangle$ state and states in the original Krylov subspace. The (unnormalized) amplitudes of this state are shown in Fig. S14(b). That this state is annihilated by $\hat{H}'$ can be seen using the transition amplitudes shown in Fig. S14(a). In presence of the diagonal terms of $\hat{H}^{(2)}_{\text{eff}}$, the eigenstates generally do not have exactly zero overlap with the other "neighbor

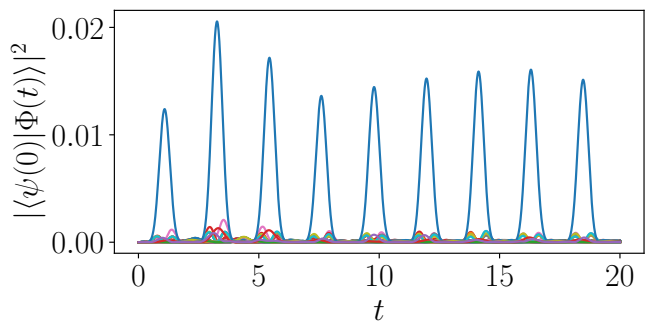

FIG. S13. Dynamics of $\hat{H}_{\text{eff}} + \hat{H}^{(2)}_{\text{eff}}$ after a quench from $|\Phi\rangle$ for $L = 20$ and $\mu = h = 1$. Shown is the overlap of the wave function with all 135 states in a Krylov sector of $\hat{H}_{\text{eff}}$ that can be reached with a single application of $\hat{H}^{(2)}_{\text{eff}}$ from the spin-1 sector. It is clear that the wave function only has nonnegligible overlap on a single state. The same picture is true in all the other similar sectors, as they are related by translation and spatial inversion.

states". Nonetheless, these other states still have very low participation in many eigenstates when μ is ≥ 0.5.

Of course, this destructive interference occurs only for states that occupy the graph symmetrically. This is true for the $|\Phi\rangle$ state, as well as when evolving the $|\Psi_2\rangle$ state, but it is not the case for $|\Psi_4\rangle$, as in one cell we only have $|\downarrow\downarrow\uparrow\downarrow\rangle$ but not its symmetric partner $|\downarrow\uparrow\downarrow\downarrow\rangle$. $|\Psi_4\rangle$ then has a strong overlap with the eigenstates of Fig. S14 that are spread evenly over the whole graph. This leads to leakage beyond the "neighbor states" and to thermalization.

VIII. OPTIMAL $|\Psi_2'\rangle$ STATES

In the main text, we have introduced the state $|\Psi_2'\rangle = (|\Psi_2\rangle - \alpha\,|\beta\rangle)/\sqrt{1+\alpha^2}$. In this section, we study the effect of α on the revival fidelity of $|\Psi_2'\rangle$. In Fig. S15(a), we see that for small values of μ we can get a clear improvement of the revivals with a value of α around 0.4. To get a more general relation between μ and α, we perform a scan and look at the average fidelity for the three first revivals. This is shown in Fig. S15(b) and we find that the optimal value $\alpha^\star$ approximately obeys $\alpha^\star(\mu) = 1/(0.46 + 2.58\mu)$. This form of scaling is expected, as the matrix elements of $\hat{H}^{(2)}_{\text{eff}}$ connecting the spin-1 sector and $|\beta\rangle$ are of order $1/\mu$. We also recover $\alpha = 0$ as $\mu = h \to \infty$, which is expected as in that case we only have $\hat{H}_{\text{eff}}$ and the dynamics is trapped in the spin-1 subspace.

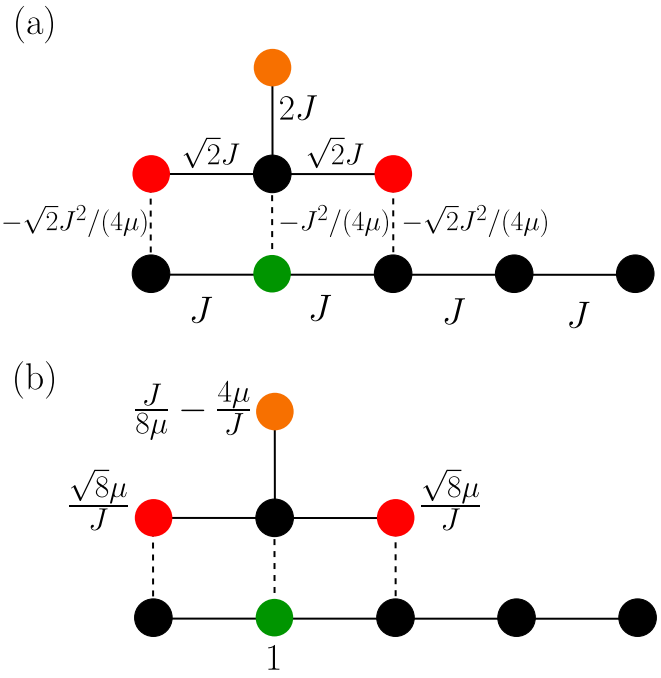

FIG. S14. Graph of the Hilbert space in the Krylov subspace generated by $\hat{H}_{\text{eff}}$ and by a single application of $\hat{H}^{(2)}_{\text{eff}}$ in the fully symmetric sector under translation by 4 sites and spatial inversion. The orange vertex corresponds to the $|\Psi_2\rangle$ state, while the $|\Phi\rangle$ state is the red vertex on the right and the $|\beta\rangle$ state is the green vertex. Since it is not fully symmetric, the $|\Psi_4\rangle$ state itself does not correspond to a single vertex, but it only has overlap with the rightmost red vertex. The full edges represent transitions allowed by $\hat{H}_{\text{eff}}$ while dashed edges are transitions enabled by $\hat{H}^{(2)}_{\text{eff}}$. The transition amplitudes are shown in panel (a). The regular structure of the graph allows atypical eigenstates which are mostly localized in the upper part of the graph. An example of such an exact eigenstate is shown in panel (b), with only four states with nonzero weight (whose unnormalized values are printed next to the corresponding vertices).

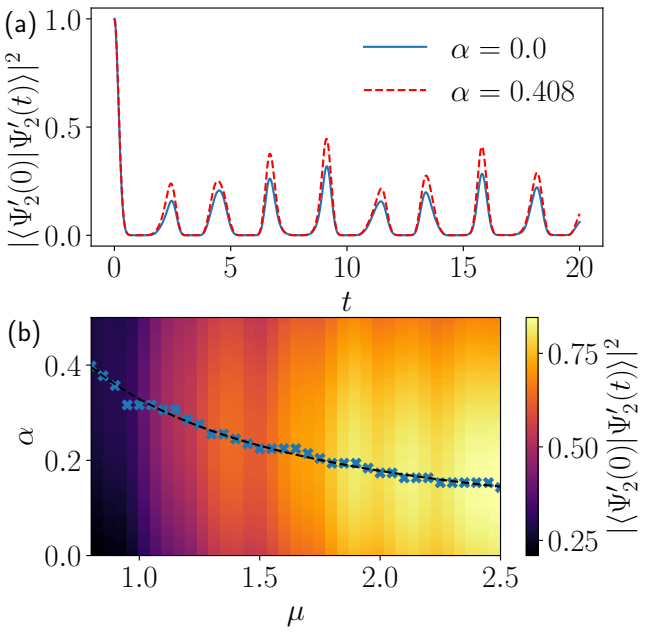

FIG. S15. Effect of α on the revival fidelity of $|\Psi_2'\rangle$ for $L = 16$. (a) Enhancement of revivals with $\alpha = 0.408$ for $\mu = h = 0.8$. (b) Average fidelity of the first three revivals (indicated by the color scale at right) for different values of α and $\mu = h$ for $L = 16$. The blue crosses show the optimal value of α for each μ while black dashed line is the fit to it $1/(0.46+2.58\mu)$.

IX. THIRD ORDER SW TERM

We can go beyond second order and look at the third order SW term:

$$
\begin{aligned}
H_{\text{eff}}^{(3)} = \frac{J^3}{32\mu^2}\Big[& \sum_{j \text{ odd}} \Big(Q_{j-1}\sigma_j^+\sigma_{j+1}^+\sigma_{j+2}^- Q_{j+3} + \text{h.c.} \\
& + P_{j-1}\sigma_j^+\sigma_{j+1}^-\sigma_{j+2}^- P_{j+3} + \text{h.c.}\Big) \\
& + \sum_{j \text{ even}} \Big(P_{j-1}\sigma_j^+\sigma_{j+1}^+\sigma_{j+2}^- P_{j+3} + \text{h.c.} \\
& + Q_{j-1}\sigma_j^+\sigma_{j+1}^-\sigma_{j+2}^- Q_{j+3} + \text{h.c.}\Big) \\
& - \sum_{j \text{ even}} \Big(\hat{P}_{j-1}\hat{X}_j\hat{Q}_{j+1}\hat{Q}_{j+2} + \hat{P}_{j-2}\hat{P}_{j-1}\hat{X}_j\hat{Q}_{j+1} \Big) \\
& - \sum_{j \text{ odd}} \Big(\hat{Q}_{j-1}\hat{X}_j\hat{P}_{j+1}\hat{P}_{j+2} + \hat{Q}_{j-2}\hat{Q}_{j-1}\hat{X}_j\hat{P}_{j+1} \Big) \Big]
\end{aligned}
\tag{S9}
$$

The terms on the two last lines are the same as in the effective Hamiltonian $\hat{H}_{\text{eff}}$ but with additional projectors on sites $j+2$ or $j-2$, and so do not cause any leakage out of the integrable subspaces. However, the terms in the first four lines do. For example, they act on $|\Psi_2\rangle = |{\downarrow}{\uparrow}{\uparrow}{\downarrow}{\downarrow}{\uparrow}{\uparrow}{\downarrow}\rangle$, taking it to $|{\uparrow}{\downarrow}{\downarrow}{\downarrow}{\downarrow}{\uparrow}{\uparrow}{\downarrow}\rangle$, $|{\downarrow}{\uparrow}{\uparrow}{\downarrow}{\uparrow}{\downarrow}{\downarrow}{\downarrow}\rangle$, $|{\downarrow}{\downarrow}{\downarrow}{\uparrow}{\downarrow}{\uparrow}{\uparrow}{\downarrow}\rangle$ and $|{\downarrow}{\uparrow}{\uparrow}{\downarrow}{\downarrow}{\downarrow}{\downarrow}{\uparrow}\rangle$. We note that $\hat{H}_{\text{eff}}^{(3)}$ has a prefactor of $J^3/(32\mu^2)$, so for $\mu \approx J$ its contribution will be small compared to that of $\hat{H}_{\text{eff}}$.

X. MATTER DYNAMICS

In this section, we briefly discuss the dynamics from the point of view of the LGT matter. As discussed in the main text, the fermion density simply corresponds to the domain wall density in our spin model as $\hat{n}_j \equiv (1 - \hat{Z}_j\hat{Z}_{j+1})/2$. We will show the dynamics of the fermions after quenches from the states $|\Psi_2\rangle$, $|\Psi_3\rangle$ and $|\Psi_4\rangle$. We focus on these states as they are product states with a small spatial periodicity. We also note that for $\mu = h \geq 2$, the $|\Psi_2\rangle$ dynamics is essentially state transfer to $|\Phi\rangle$ and back. So the dynamics from $|\Phi\rangle$ would be the same but shifted in time by a half-period.

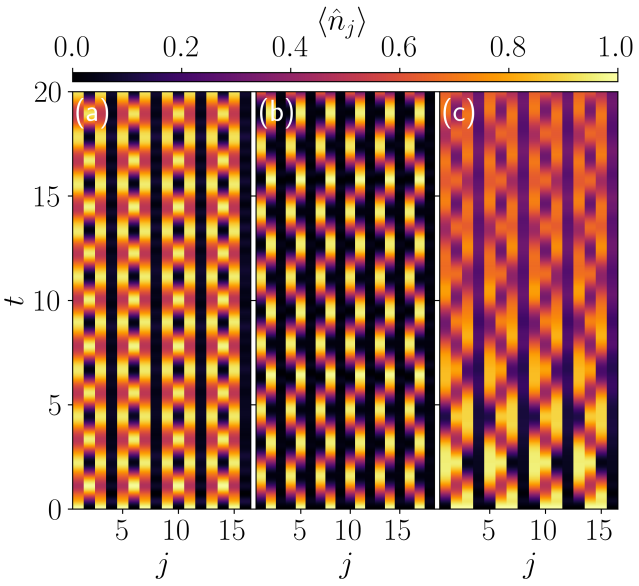

FIG. S16. Dynamics of the fermion density after a quench from (a) $|\Psi_2\rangle$, (b) $|\Psi_3\rangle$ and (c) $|\Psi_4\rangle$. All panels are for $\mu = h = 2$, while $L = 16$ for panels (a) and (c) but $L = 18$ for panel (b).

In Fig. S16, we show the fermion density dynamics for $\mu = h = 2$. As expected, for such a large value of the parameters, the dynamics is essentially that of multiple independent cells separated by frozen empty sites. However, for $|\Psi_4\rangle$ we do see the effects of interactions between cells at later times. For $|\Psi_2\rangle$, each cell has three sites and oscillates between $|{\bullet}{\circ}{\bullet}\rangle$ and $(|{\circ}{\bullet}{\bullet}\rangle + |{\bullet}{\bullet}{\circ}\rangle)/\sqrt{2}$. For $|\Psi_4\rangle$ each three-site cell oscillates between $|{\circ}{\bullet}{\bullet}\rangle$ and $|{\bullet}{\bullet}{\circ}\rangle$. Finally, for $|\Psi_3\rangle$ each cell has two sites and the oscillations are simply between $|{\circ}{\bullet}\rangle$ and $|{\bullet}{\circ}\rangle$.

We can also wonder what happens for smaller values of $\mu = h$. This is shown in Fig. S17. The empty sites between active cells are no longer frozen but show oscillations for $|\Psi_2\rangle$ and $|\Psi_3\rangle$. This is a sign that the cells are no longer isolated but instead interact. Importantly, these oscillations of the previously frozen sites show no clear damping which would be indicative of thermalization. On the other hand, for $|\Psi_4\rangle$ we see that the sites between cells gradually fill up and that the dynamics leads

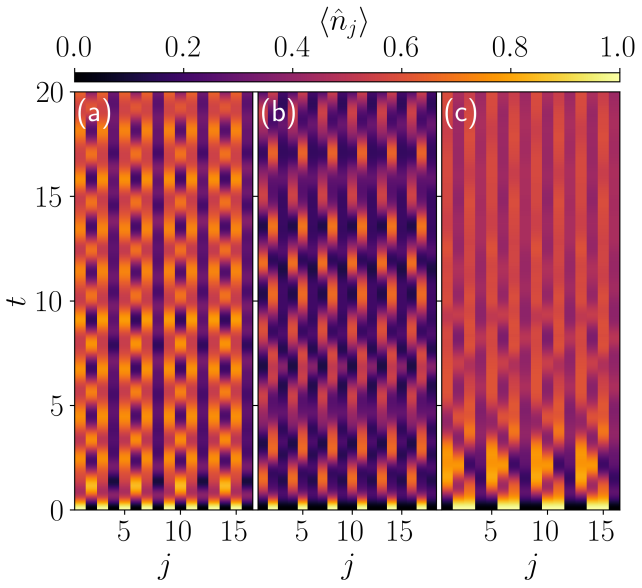

FIG. S17. Dynamics of the fermion density after a quench from (a) $|\Psi_2\rangle$, (b) $|\Psi_3\rangle$ and (c) $|\Psi_4\rangle$. All panels are for $\mu = h = 0.8$, while $L = 16$ for panels (a) and (c) but $L = 18$ for panel (b).

to thermalization.

While the equilibrated expectation values still show imbalance between the occupation of odd and even matter sites, this does not denote ergodicity breaking as the Hamiltonian itself is only invariant under translations by two sites. To test if $|\Psi_2\rangle$ thermalizes, we look at the fermion imbalance defined as

$$\hat{n}_{\text{Imb}} = \frac{2}{L}\left(\sum_{j \text{ odd}} \hat{n}_j - \sum_{j \text{ even}} \hat{n}_j\right). \tag{S10}$$

In Fig. S18, we show the dynamics of this quantity after quenches from the $|\Psi_2\rangle$ and $|\Psi_4\rangle$ states. We do not show it for $|\Psi_3\rangle$ as it is always zero for symmetry reasons. As expected, we see that $|\Psi_2\rangle$ exhibits oscillations in the imbalance that are much more pronounced and long-lived than for $|\Psi_4\rangle$. Perhaps more surprisingly, we see that the center of the oscillations and the late-time values also differ between the two states. For $|\Psi_4\rangle$, both of them agree well with the prediction of the canonical ensemble. This value is computed at the energy density of $|\Psi_2\rangle$ and $|\Psi_4\rangle$ (which are identical) and in the relevant symmetry sectors. We see that $|\Psi_4\rangle$ clearly thermalizes at late times with no apparent breaking of ergodicity. Meanwhile, for $|\Psi_2\rangle$ this is only the case when $\mu = h$ is very small. Even for $\mu = h = 0.5$, there is still a noticeable difference between the equilibration value of the imbalance and the canonical ensemble prediction. This further highlights the clear difference between $|\Psi_2\rangle$ and $|\Psi_4\rangle$. While the latter only shows non-thermal dynamics at shorter time due to the integrability of $\hat{H}_{\text{eff}}$, the former shows actual many-body scarring because of the interplay of $\hat{H}_{\text{eff}}$ with the higher-order SW terms.

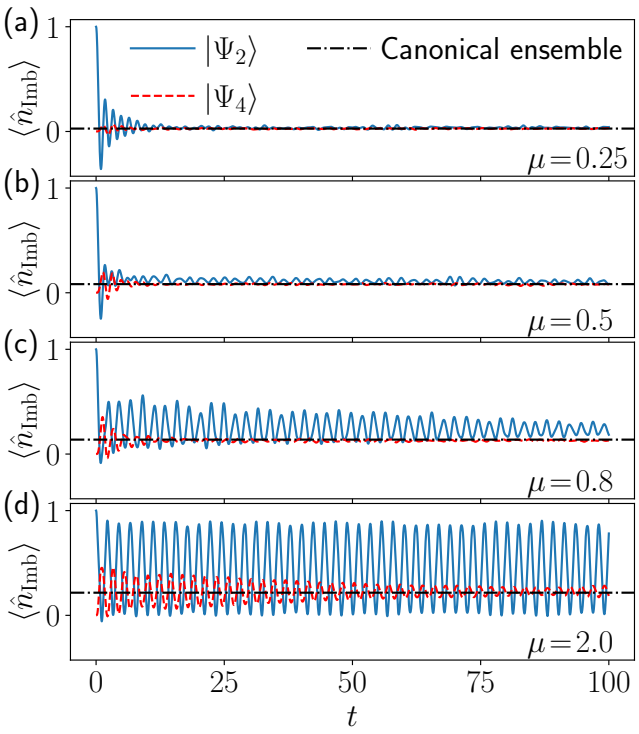

FIG. S18. Dynamics of the fermion imbalance after a quench from $|\Psi_2\rangle$ and $|\Psi_4\rangle$ for various values of $\mu = h$ and $L = 16$.